FRICTION AND WEAR OF 20% VOLUME FRACTION SUBMICRON Al_2O_3/6061 ALUMINUM ALLOY COMPOSITE FOR BRAKE SYSTEM APPLICATION

BY

MIRZA MURTUZA ALI BAIG

A Thesis Presented to the

DEANSHIP OF GRADUATE STUDIES

KING FAHD UNIVERSITY OF PETROLEUM & MINERALS

DHAHRAN, SAUDI ARABIA

In Partial Fulfillment of the

Requirements for the Degree of

MASTER OF SCIENCE

In

MECHANICAL ENGINEERING

JANUARY 2009

KING FAHD UNIVERSITY OF PETROLEUM AND MINERALS

DHAHRAN 31261, SAUDI ARABIA

DEANSHIP OF GRADUATE STUDIES

This thesis, written by **Mirza Murtuza Ali Baig** under the direction of his thesis advisor and approved by his thesis committee, has been presented to and accepted by the Dean of Graduate Studies, in partial fulfillment of the requirements for the degree of **MASTER OF SCIENCE IN MECHANICAL ENGINEERING**.

Thesis Committee

Dr. Amro M. Al- Qutub (Advisor)

Dr. Ibrahim M. Allam (Member)

Dr. Nesar Merah (Member)

Dr. Amro M. Al- Qutub
Department Chairman

Dr. Salam A. Zummo
Dean of Graduate Studies

14/4/09

Date

عمادة الدراسات العليا
DEANSHIP OF GRADUATE STUDIES

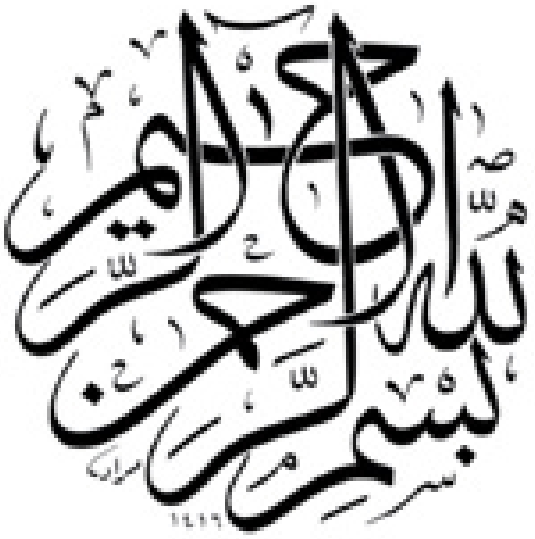
بسم الله الرحمن الرحيم

Dedicated to

My beloved Parents, Brothers and Fiancée

ACKNOWLEDGEMENTS

All praise and thanks are due to Almighty Allah, Most Gracious, Most Merciful, for the immense mercy which has resulted in my accomplishing this research. May peace and blessings be upon the prophet Muhammad (PBUH), his family and his companions.

First, I would like to acknowledge KFUPM for the support extended towards my research through its remarkable facilities and for providing me the opportunity to pursue graduate studies.

My parents have always been there for me in my good and difficult times. They have supported me in everything that I have endeavored, and their continual encouragement helped me to complete this task. My family has always been a pillar of support for me, especially my father. His continuous encouragement and motivation lifted my confidence whenever I encountered problems. Words fall short in conveying my gratitude towards them. A prayer is the simplest means I can repay them - May Allah (S.W.T.) give them good health and give me ample opportunity to be of service to them throughout my life.

I would like to express my profound gratitude and appreciation to my advisor Dr. Amro Al-Qutub for his consistent help, guidance and attention throughout this research. His valuable suggestions and useful discussions made this work interesting to me. Special and sincere thanks go to my thesis committee members Dr. Ibrahim M. Allam and Dr. Nesar Merah for their interest, cooperation and constructive advice.

I would also like to thank all faculty and staff members in the Mechanical Enginering department, especially Dr. Antar, Mr. Faheem Patel, Mr. Saleh, Mr. Romeo, Mr. Saber Ali and Mr. Abdul Azeez, for their kind support and continuous cooperation.

I would like to thank my seniors and colleagues, Fareed Bhai, Rizwan Bhai, Shujath, Sarfaraz, Hasan, Asrar, Nizam, Omer, Hussain, Ammar, Abdul Rahman, Misbha, for their concern and help. I would also like to thank my friends Saleem, Faizal, Faizan, Siraj, Ilyas, Shafeeq, Waseem, Mujahid, Abdul Muqtadir, Imran Ghani, Abdul Hafeez, Nazeer, Abdul Malik, Shaik Imran, ABR, Rizwan Farooqi, Safi, Naseer and Irfan among many others who have been like a second family to me here in KFUPM. I am indebted to my roommates Shaik Rizwan and Mumtaz for their wonderful companionship. I am also grateful to my cousins Mr. Faizullah and Mr. Sajid and to their families for their concern and help.

TABLE OF CONTENTS

LIST OF TABLES

LIST OF FIGURES

THESIS ABSTRACT (ENGLISH)

NAME: MIRZA MURTUZA ALI BAIG

TITLE: FRICTION AND WEAR OF 20% VOLUME FRACTION SUBMICRON Al_2O_3/6061 ALUMINUM ALLOY COMPOSITE FOR BRAKE SYSTEM APPLICATION

MAJOR: MECHANICAL ENGINEERING

DATE: JANUARY, 2009

Metal matrix composites (MMCs) containing hard particulates offer superior operating performance and resistance to wear. The strengthening of aluminum alloys with a dispersion of fine ceramic particulates has dramatically increased their potential for wear resistance applications. One of these applications is the development of aluminum matrix composite (AMC) brake discs, favored primarily over cast iron for their high thermal conductivity and low density. Consequently, these materials tend to be lighter in weight and harder than the traditional cast iron brake discs. Therefore they offer potential for reducing braking system weight, improving the friction coefficient and possibly increasing the wear life of brake components as well. Friction and wear performance are the most important considerations in the design of MMC brake discs, and it is the investigation of the interdependence of these two properties that comprise the bulk of this work.

There have been studies which concentrated on the investigation of wear behavior of SiC particulate reinforced aluminum alloys for disc brakes. However, no published data have been found which aimed to delineate the tribological performance of submicron Al_2O_3 reinforced aluminum alloys. The prime objective of this work is to evaluate the friction and wear characteristics of 20% volume fraction sub-micron Al_2O_3 reinforced 6061 Al composite as a brake counter face. These characteristics are evaluated at varying loads and sliding speeds at room temperature in dry sliding conditions. The results are compared with gray cast iron under similar conditions. The average wear rate of AA6061/Al_2O_3/20p composite is found to be 18% lower than that of gray cast iron sliding against semi-metallic brake pad material. The average wear rate for brake pad material is found to be 31% lower while sliding against AA6061/Al_2O_3/20p composite than sliding against gray cast iron. The proposed aluminum composite is found to be a better candidate for brake rotor applications.

MASTER OF SCIENCE DEGREE

KING FAHD UNIVERSITY OF PETROLEUM and MINERALS

Dhahran, Saudi Arabia

THESIS ABSTRACT (ARABIC)

ملخص الرسالة

الاسم: ميرزا مرتضى علي بيج

عنوان الرسالة: الاحتكاك و التأكل للألومنيوم 6061 المقوى بنسبة 20% من Al_2O_3 تحت الميكرون من أجل تطبيقات أنظمة الفرامل

التخصص: الهندسة الميكانيكية

التاريخ: يناير ، 2009

مصفوفات المعادن المركبة (MMC'S) التى تحتوى على جزيئات صلبة تعطى أداء تشغيلى فائق و مقاومة للتأكل و عملية تقوية سبائك الالومنيوم بجزىئات سيراميك دقيقة تؤدى الى زيادة كبيرة فى امكانية استخدامها فى التطبيقات المقاومة للتأكل وإحدى هذه التطبيقات هى تطوير مصفوفة ألومنيوم مركبه (AMC) لأقراص الفرامل والتى تتميز عن الحديد الزهر بتوصيل حرارى عالى و كثافة منخفضة و بالتالى وزنها أقل وأكثر صلابه من الفرامل المصنعة من الحديد الزهر و هذا يعطيها امكانية عالية لتقليل وزن منظومة الفرامل و تحسين معامل الاحتكاك و زيادة عمر التأكل لمكونات الفرامل. من ناحية الصيانة فإن تأكل مادة كل من العضو الدوار و الفرامل هام جدا و هناك العديد من الدراسات التى ركزت على بحث سلوك التأكل بالنسبة لأقراص الفرامل المصنعة من سبائك الالومنيوم المقواه بجزيئات SiC (8 to 43 μm).

دمج جزىئات سيراميك كبيرة الحجم نسبيا يقلل من معدل التأكل للأجزاء الدوارة من الفرامل و يحسن من تأكل بطانة الفرامل و لكن لم يتم العثور على بيانات منشورة تهدف الى وصف الاداء التريبولوجى لسبائك الالومنيوم Al_2O_3 تحت الميكرون المقواة. كان من المتوقع عند تقليل حجم جزيئات السيراميك الكبيرة نسبيا الى ما تحت الميكرون فى مركب الجزء الدوار أن يقل معدل التأكل لنظام الفرامل وأن يزيد ذلك من عمر أجزاء الفرامل و على هذا فإن الهدف الرئيسى من هذا البحث هو تقييم خصائص الاحتكاك و التأكل للألومنيوم 6061 المقوى بنسبة 20% من Al_2O_3 تحت الميكرون وإختبارها عندما تنزلق ضد مادة فرامل تجارية شبه معدنية. و قد تم دراسة هذه الخصائص عند أحمال و سرعة إنزلاق متغيرة عند درجة حرارة الغرفة لشروط الإنزلاق الجاف و تم مقارنة النتائج مع الحديد الزهر الرمادى عند نفس الظروف و قد اتضح ان الألومنيوم المركب المقترح مرشح أفضل لتطبيقات فرملة الجزء الدوار بالإضافة الى معدل تأكل أقل لسطح و مادة الفرامل.

درجة شهادة الماجستير

جامعة الملك فهد للبترول و المعادن

الظهران, المملكة العربي السعودية

NOMENCLATURE

MMC	Metal matrix composite
AMC	Aluminum matrix composite
AA6061/Al_2O_3/20p	Composite based upon 6061 aluminum alloy containing 20% volume fraction particulates of Al_2O_3.
ρ	Density
V	Volume
L	Length
N	number of revolutions per minute
R	Wear track radius
m	Mass
d	Diameter
B	Bias error
P	Precession error
U	Uncertainty
S	Sliding distance
t	Time
v	Velocity
F_C	Calibration load
w	Wear rate
F_N	Normal reaction
F_μ	Frictional force
L_C	Distance of load cell from shaft axis

CHAPTER 1

INTRODUCTION

1.1 Background

When a brake is applied, all of the kinetic energy of the vehicle is converted into thermal energy.

Energy (Heat) Factors:

$E = 1/2\ mv^2$

where

E = Kinetic energy generated

m = Vehicle weight

v = Speed of the vehicle

Therefore, the brake power required to stop the vehicle is directly proportional to the vehicle weight. Thus if the weight of the vehicle is doubled, the energy of motion (converting to heat) is doubled. The effect of vehicle speed is even more serious. If the speed of the vehicle is doubled, the brake system would require four times the energy to stop the vehicle, which means the brake mechanism must absorb and dissipate four times as much heat.

The total energy resulting from the increase of vehicle weight and speed is multiplied, i.e. if both the weight and speed of a vehicle are doubled then the brake system would require to generate eight times more power or to absorb and dissipate eight times more heat.

The amount of heat generated by brake applications is usually more than a brake mechanism can absorb and dissipate. This will result in brake temperature increase. In normal brake applications, the time interval between brake applications (brake cycles) allows the heat to cool off. However, if repeated abrupt or panic stops are made within very short time intervals, the brake temperature will continue to rise. This will result in brake fade or brake failure, and it will damage the brake system including brake, rotors or drums, calipers, and fluid.

Since all the converted heat needs to be absorbed and dissipated, the rotor comes into play as the "heat sink" – similar to a water sink. As the rotor heats up, it absorbs heat just like a water sink holds water from a faucet. If the water pours into the sink faster than the drain can handle, the water will overflow. Likewise, if the temperature of the rotor increases faster than the rotor can cool down, consequent damages are likely to occur. In one case we get with a wet floor, and in the other a damaged brake system. In some extreme cases with too much heat, the tires may be set on fire. Therefore, a bigger heat "sink" and efficient heat "draining" system to prevent heat from overflowing.

Increasing the holding (thermal) capacity means enlarging the "sink" size, but in a brake rotor this may be impractical, as it would also increase the rotating mass, which

slows down the acceleration and deceleration. This is not a desirable solution. So the challenge is to produce a rotor with a smaller mass, yet able to manage or hold the same amount of heat longer, without overflow. To achieve this goal, there are two main issues to overcome:

1. A better material that is more resistant to higher temperature with good thermal stability
2. Improved wear resistant material.
3. Improved heat capacity.

Great efforts are being made around the world by different automobile manufacturers on the possibility of using aluminum metal matrix composite (AMC) brake discs in place of conventional gray cast iron brake discs. All those efforts are undertaken with the prime aim of utilizing the favorable characteristics of AMCs such as high thermal conductivity and low density when compared with cast iron. Thermal conductivity and expansion of AMC brake components can be tailored easily by adjusting the level and distribution of the particulate reinforcement. Thus, the silicon carbide reinforced aluminum composites are increasingly used as substitute material for cylinder heads, liners, pistons, brake rotors and calipers.

Metal matrix composites (MMCs) refer to a kind of material in which rigid ceramic reinforcements are embedded in a ductile metal or alloy matrix. MMCs combine metallic properties (ductility and toughness) with ceramic characteristics (high strength and modulus), leading to greater strength in shear and compression and to higher service temperature capabilities [1, 2].

The metal matrix is made of a specific metal or metal alloy. The matrix serves as the binder to hold the reinforcement together and to distribute the improved properties, attained via the reinforcement, uniformly or in a specified direction. The total dependency of the composite upon the matrix varies with the combination of matrix and reinforcement type, as well as the combining process used [3]. The use of continuous fibers as reinforcements may result in the transfer of most of the load to the reinforcing filaments, and hence the composite strength will be governed primarily by the fiber strength. The primary roles of the matrix alloy then are to provide an efficient transfer of the load to the fibers and to blunt cracks in the event of fiber failure. So the matrix alloy for a continuously reinforced MMC may be chosen more for toughness than for strength. On this basis, lower-strength, more ductile, and tougher matrix alloys may be utilized in continuously reinforced MMCs. For discontinuously reinforced MMCs, the matrix may govern composite strength. Then, the choice of matrix will be influenced by consideration of the required composite strength, and higher-strength matrix alloys may be required [4].

Reinforcement materials in MMCs are second-phase additions to a metallic matrix that result in some net property improvement, a typical one being an increase in strength. Generally, most reinforcement materials for MMCs are ceramics (oxides, carbides, nitrides, and so on) which are characterized by their high strength and stiffness at both ambient and elevated temperatures. Examples of common MMC reinforcements are SiC, Al_2O_3, TiB_2, B_4C, and graphite. Metallic reinforcements are used less frequently.

The role of the reinforcement varies with its type in structural MMCs. In particulate and whisker-reinforced MMCs, the matrix is the major load-bearing constituent. The role

of the reinforcement is to strengthen and stiffen the composite by preventing matrix deformation by mechanical restraint. This restraint is generally a function of the interparticle spacing-to-diameter ratio. In continuous fiber reinforced MMCs, the reinforcement is the principal load-bearing constituent. The metallic matrix serves to bond the reinforcement, and it transfers and distributes the load. Discontinuous fiber reinforced MMCs display characteristics between those of continuous fiber and particulate reinforced composites. Typically, reinforcement increases the strength, stiffness and temperature capability of MMCs. When combined with a metallic matrix of higher density, the reinforcement also reduces the density of the composite, thus enhancing properties such as specific strength [4].

The wide selection of matrices and reinforcements permits the development of application-tailored MMCs. For example, aircraft electronic packaging components require a low coefficient of thermal expansion (CTE), high thermal conductivity (TC), and low density. Except beryllium, no metals have all three properties. Since beryllium is very expensive and is toxic, MMCs are a viable alternative. By combining ultra-high modulus graphite fibers with aluminum, a composite can be manufactured to meet these three requirements simultaneously.

Particle or discontinuously reinforced MMCs have become very important, because they are inexpensive vis à vis continuous fiber reinforced composites, and they have relatively isotropic properties compared to fiber reinforced composites.

Aluminum, the second most plentiful metallic element on earth, became an economic competitor in engineering applications in the late 19^{th} century. Aluminum alloys have

been used for tribological applications since 1940, when cast aluminum-tin bearings were introduced for heavy machinery [5]. The Al alloys are attractive due to their low density, their capability to be strengthened by precipitation, their good corrosion resistance, their high thermal and electrical conductivity, and their high damping capacity [6]. Aluminum matrix composites (AMCs) have been widely studied since the 1920s, and they are now used in sporting goods, electronic packaging, armours and automotive industries. They offer a large variety of mechanical properties depending on the chemical composition of the Al matrix. They are usually reinforced by Al_2O_3, SiC, C but SiO_2, B, BN, B_4C, AlN may also be considered. The aluminum matrices are in general Al-Si, Al-Cu, 2xxx or 6xxx alloys. As proposed by the American Aluminum Association, the AMCs should be designated by their constituents: accepted designation of the matrix/abbreviation of reinforcement's designation/arrangement and volume fraction in % with the symbol of type (shape) of the reinforcement. For example, an aluminum alloy AA6061 reinforced by particulates (P) of alumina (Al_2O_3), 22% volume fraction, is designated as "AA6061/Al_2O_3/22P".

In the 1980s, transportation industries began to develop discontinuously reinforced AMCs. They are attractive for their isotropic mechanical properties (higher than their unreinforced alloys) and their low costs (cheap processing routes and low prices of the discontinuous reinforcement such as SiC particles or Al_2O_3 short fibers).

It is highly desired to improve the fuel consumption rate by a reduction in total weight of vehicles. The brake rotor accounts for a large part of the total chassis weight. Research and development has been carried out to substitute the conventional cast iron brake rotor with an aluminum brake rotor [7, 8]. Thus the silicon carbide reinforced

aluminum composites are increasingly used as substitute materials for cylinder heads, liners, pistons, brake rotors and calipers [9].

Among the various and numerous applications, a few arbitrary examples are: (1) Brake rotors for German high speed train ICE-1 and ICE-2 developed by Knorr Bremse AG and made from a particulate reinforced aluminum alloy (AlSi7Mg+SiC particulates) supplied by Duralcan. Compared to conventional cast-iron parts with 120kg/piece, the 76kg of the AMC rotor offers an attractive weight saving potential. (2) The braking systems (discs, drums, calipers or back-plate) of the New Lupo from Volkswagen are made from particulate reinforced aluminum alloy supplied by Duralcan.

1.2. Processing routes

A crucial step in the processing of MMCs reinforced with ceramic particles is the insertion of ceramic particles in the metal matrix alloy. This greatly influences the strength of the composite, since it is controlled by the metal-particle interfacial bond strength. The most important aspect of the microstructure is the distribution of the reinforcing particles, and this depends on the processing and fabrication routes involved, as well as the relative size of the matrix and reinforcing particles. Quality control objectives include the elimination of excessive interfacial reaction during processing, particularly for melt routes, and also the avoidance of microstructural defects such as poor interfacial bonding, internal voids and clustering of the reinforcement. Particulate MMCs are most commonly manufactured, either by melt incorporation and casting technique, or by powder blending and consolidation. Other routes include reactive

processing or spray co-deposition. An overview of the common processing routes employed to produce MMCs is discussed in the following section.

1.2.1 Stir casting

Stir casting involves stirring the melt with solid ceramic particles and then allowing the mixture to solidify. This can usually be done by using fairly conventional processing equipment, and it can be carried out on a continuous or semi-continuous basis. A concern is to ensure that good particle wetting occurs. Difficulties can arise from the increase in viscosity on adding particles or, especially, fibers to a melt. The viscosity should be sufficiently low to allow casting operations to be carried out. Also, microstructural inhomogeneities can also arise, notably that of particle agglomeration and sedimentation in the melt. Redistribution as a result of particle pushing by an advancing solidification front can also be a problem.

Stir casting usually involves prolonged liquid-ceramic contact at high temperatures, which can cause substantial interfacial reaction. This has been studied in detail for Al-SiC alloys which are predominant among cast aluminum alloys, in which the formation of Al_4C_3 and Si can be extensive [10]. This both degrades the final properties of the composite and raises the viscosity of the slurry, making subsequent casting difficult. The rate of reaction is reduced, and it can become zero if the melt is Si-rich. The reaction kinetics and Si levels needed to eliminate it are such that it has been concluded that the casting of Al-SiCp involving prolonged melt-holding operations is suited to conventional (high Si) casting alloys, but not to most wrought alloys. The presence of silicon in aluminum significantly reduces the tendency of aluminum to react chemically with SiC

and to form Al_4C. This latter compound severely embrittles SiC-reinforced Al MMCs, even when present in small quantities [11].

1.2.2 Powder metallurgy

Powder metallurgy is a common route for the preparation of discontinuously reinforced MMCs. Because of the difficulty in wetting ceramic particles with molten metal, the Powder Metallurgy or PM route was developed [12]. In this process, powders of the metallic matrix and reinforcement are first blended and fed into a mold of the desired shape. Blending can be carried out dry or in liquid suspension. Pressure is then applied to further compact the powder (cold pressing). The compact is then heated to a temperature which is below the melting point but high enough to develop significant solid-state diffusion (sintering). After blending, the mixture can also be consolidated directly by hot pressing or hot isostatic pressing (HIP) to obtain high density. The consolidated composite is then available for secondary processing. Achieving a homogeneous mixture during blending is a crucial factor because the discontinuous reinforcement tends to persist as agglomerates with interstitial spaces too small for penetration of matrix particles [4].

The PM route for manufacturing MMCs offers some advantages compared with ingot metallurgy or diffusion welding, especially the low manufacturing temperature that avoids strong interfacial reaction, minimizing the undesired reactions between the matrix and the reinforcement. Composites that use particles or whiskers as reinforcement can be obtained more easily by PM than by other alternative routes. Moreover, particles are cheaper than continuous fibers of the same composition. Another advantage of PM is the

uniformity in the reinforcement distribution. This uniformity improves not only the structural properties but also the reproducibility level in the properties [6].However, the only mechanical property that is adversely affected is the elongation, which is almost always decreased, due mainly to the higher number of nucleation sites present for the cracks to form [12].

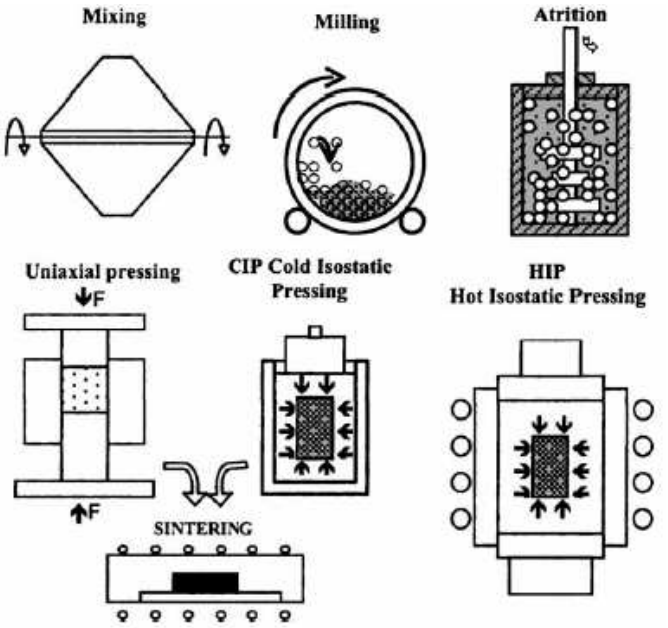

Figure 1.1 Conventional PM process [13]

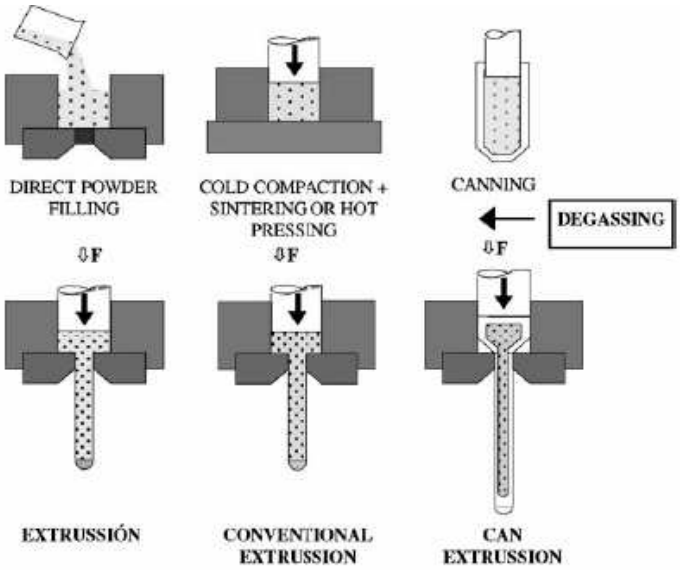

Figure 1.2 PM extrusion process [13]

1.3. Friction material

Friction materials are used to induce friction in applications when slow or decreasing movement is desired, such as in brakes and clutches. The main purpose of a car brake is to reduce the speed. In this process, the kinetic energy is transformed into heat by the frictional work. Brake linings can be grouped into three key categories. These are metallic, semi-metallic and non-asbestos organic.

Table 1.1: Classification of brake pads

Classification	Ingredients
Metallic	Predominantly metallic, such as steel fibres, copper fibres, etc.
Semi-metallic	Mixture of metallic and organic ingredients
Non-asbestos organic	Predominantly organic, such as mineral fibres, rubber, graphite, etc.

Semi-metallic linings are a mixture of fragments or powdered metal held together with phenolic resins and other binders and fillers. The metal is present for heat transfer, and the amount present depends upon the specific heat transfer requirements. In some brake linings, iron and steel (e.g., steel wool and iron sponge) and titanium are used (high heat transfer coefficients). In situations which are not so demanding, such as the rear disc brakes of normal cars, the pads may contain softer metals such as copper and brass. Because a single material cannot successfully meet friction material's general-purpose

requirements, automotive friction material usually consists of several ingredients bound into a composite. They are often categorized into four classes [14-16] as follows:

1.3.1 Binder

The purpose of a binder is to maintain the brake pads' structural integrity under mechanical and thermal stresses. The different types of binders include phenolic resin, COPNA resin, silicone-modified resin, cyanate ester resin, epoxy-modified resin, and thermoplastic polyimide resin.

1.3.2 Reinforcing fibers

Metallic chips or granules are commonly used as reinforcing fibers, and hence they are referred to as metallic 'fibers' although they may not be strictly thread-like. Examples of metallic fibers include steel, brass and copper. The drawback of using steel fibers is that they rust, especially if the vehicle has an extended rest period or if the vehicle is used near a coastal environment. Steel fibers attacked by rust will be less resilient, thereby compromising their functionality as reinforcing fibers. Therefore, certain brake pads include metals such as zinc, distributed over the cross-section of the friction lining, thereby forming a sacrificial anode for rusting to occur. On the other hand, a significant advantage of using metal fibers is that they have very high conductivities and they are able to remove heat from the frictional surfaces very quickly.

1.3.3 Fillers

Fillers are added, and these appear to include clay and calcium carbonate. Sometimes referred to as 'space fillers', the fillers in a brake pad are present for the purpose of

improving its manufacturability as well as to reduce its overall cost. Calcium carbonate, for example, imparts heat stability to the friction material, thereby improving the friction material's brake fade properties. It is the cheaper of the two, but it is not as stable.

1.3.4 Frictional additives

Frictional additives are components added to brake friction materials in order to modify the friction coefficients as well as the wear rates. They are divided into two main categories: lubricants, which decrease the friction coefficients and wear rates; and abrasives, which increase friction coefficients and wear rates. Metal sulphides appear to be better lubricants than graphite. Because of the current high-energy braking demands in the vehicles, the low bonding strength between graphite and phenolic-based resin (most common binder) would result in accelerated wear of the friction material. Metal sulphides do not suffer this problem, although the toxicity of certain compounds such as lead and antimony sulphides is a disadvantage. Therefore safer alternatives such as tin and copper sulphides would be ideal as lubricants.

Semi-metallic friction materials offer stable friction, improved fade resistance and durability, and rotor compatibility. A variety of friction materials are available for many different uses. It is necessary to know the specific requirements before purchasing any friction material. Different materials have different coefficients of friction. For example, it is important to have a material that creates a large amount of friction if quick stopping is an issue. Likewise, if a great deal of heat is going to be produced during the braking, it is important to have materials that have a high energy absorption rate (high heat conductivity and heat capacity), such as semi-metallic materials.

1.4 Friction and wear

Almost all mechanical systems, artificial or natural, involve the relative motion of solid components. Whenever two surfaces slide or roll against each other, there will be frictional resistance, and wear will occur. The response of materials to this kind of interaction, often termed tribological, depends not only on the precise nature of the materials, but also on detailed conditions of the contact between them and of the motion. Friction and wear are system responses, rather than material properties. The measurement of tribological behavior therefore poses particular challenges, and a keen awareness of the factors that influence friction and wear is essential [17].

Wear can be defined as damage to a solid surface, generally involving progressive loss of material, due to relative motion between that surface and a contacting substance or substances. Materials in contact are subjected to relative motion in many different applications: for example in rotating plane bearings, pistons sliding in cylinders, and automotive brake discs interacting with brake pads [17]. Wear is controlled by the type of interacting materials, the environment, the loading condition and the type of sliding interaction [18].

In situations involving sliding or rolling contact, a companion term with wear is friction. Friction is the force that occurs at the interface between two contacting bodies. Friction acts tangential to the interface, and its direction is opposite to the motion or the incipient motion [19].

The wear may be classified in terms of the appearance of the wear scar, the physical mechanism that removes the material or causes the damage, and the conditions

surrounding the wear situation. Examples of terms in the first category are pitted, spalled, scratched, crazed, fretted, gouged, and scuffed. Terms like adhesion, abrasion, delamination, oxidative are examples of the second category. Examples of the third category are lubricated wear, unlubricated wear, metal-to-metal sliding wear, rolling wear, high stress sliding wear, and high temperature metallic wear [19].

1.4.1 Generic type of wear mechanisms

Adhesion: When two surfaces come into contact, they adhere to one another at localized sites. As the two surfaces move relative to one another, adhesion wear occurs by one surface pulling the material out of the other surface at these sites [17].

Abrasion: Abrasive wear occurs when a surface slides against harder particles. These particles may be loosely held between two sliding surfaces, or they may be a part of the second surface. Consequently, there are two types of abrasion. Two-body abrasion happens when the wear is caused by protuberances on a surface or hard particles fixed to it. Three-body abrasion occurs when the particles are not attached but between the surfaces. Abrasive wear mechanism takes place by the micro-cutting of small chips by the harder particles acting as cutting tools [18].

Fatigue: With repeated rolling, sliding and impacting, material in contact with surfaces experiences cyclic stresses. This stress cycling initiates cracks or damage on the surface. With further cycling, the cracks propagate, eventually intersecting with the surface and themselves. Free particles will be produced as a result of the crack network. Cracks, crack propagation, delamination, progressive plastic deformation and platelet wear debris are observed when fatigue wear occurs [20].

Oxidative: For dry sliding and under light loads, metallic wear scars tend to exhibit a smooth, glassy appearance. Under these conditions, the wear rate is generally low, and fine wear particles of metallic oxides are observed. The glassy appearance in these cases has been shown to be associated with the formation of an oxide layer on the surface of the wear scar. Wear then occurs by one of the three mechanisms, either in this reacted layer or at the interface between the layer and the parent material. However, between contacts, the oxide regrows on these denuded areas of the surface, and it is again removed with subsequent asperity engagement [20].

The term oxidation is used to imply any chemical reaction altering the composition of the surface. It is not limited to effects from exposure to oxygen, though this is very common in many engineering applications. Alternate terms for oxidative wear are chemical wear and corrosive wear.

1.5. Objectives

Limited work has been conducted until now in investigating the tribological behavior of 6061 Al/Al_2O_3 particulate reinforced composite against commercially available brake material. Thus, the main objective of the present investigation is to evaluate the performance of 6061 Al composite reinforced with 20% volume-fraction submicron Al_2O_3 as a brake rotor material under dry sliding conditions. This will be achieved by evaluating the wear rate of composite as well as brake material sliding against each other. The results will be compared with gray cast iron (regular brake disc material) for the same conditions. Friction coefficients for both composite and gray cast iron will be evaluated. Normal stress and sliding velocity will be used as variables. The worn surfaces

will be examined by using scanning electron microscopy (SEM). The interface temperatures will be recorded close to the contact surface by using a thermocouple.

The rest of the chapters are organized as follows. In Chapter 2, the improvement in friction and wear performances of particulate reinforced AMCs is highlighted. State-of-the-art application of AMCs for brake rotors is established. The importance of using sub-micron particulate reinforcement is discussed. Chapter 3, specifies the materials used in the present study. Sample preparation, experimental setup, experiment matrix and testing procedures are discussed. Uncertainty analysis for density and wear measurement are also included. In Chapter 4, results of dry friction and wear for the proposed Al composite and gray cast iron sliding against semi-metallic brake pad material are presented. Also, SEM micrographs of worn surfaces with the EDX analysis results are presented. Friction and wear performances of the proposed Al composite and gray cast iron are also compared. This comparison evaluates the possibility of using the proposed Al composite for brake rotor applications. Chapter 5 is the conclusion of the present work, and some future research directions are proposed.

CHAPTER 2

LITERATURE REVIEW

Metal matrix composites (MMCs) are considered as a class of materials that seek to combine the high strength and stiffness of a ceramic with the damage tolerance and toughness provided by a metal [21]. Kaczmar et al [18] reported that the reinforcing of a matrix results in increased mechanical properties and improved development properties such as fatigue strength and resistance to wear. Additionally, the thermal stability of the composite materials is improved due to the effect of the reinforcing fibers content on thermal expansion. Yu et al [19] demonstrated, by using the finite element analysis, that detailed geometrical parameters of the reinforcement as well as its volume fractions are significant for designing the composite to achieve better mechanical properties.

Among all the MMCs, aluminum may be the metal most widely used as matrix, due to its low density coupled with high stiffness [1,4]. Among all the aluminum alloys, Al 6061 possesses excellent formability in addition to high strength and good corrosion resistance. Hence, it is the most desirable matrix alloy for aluminum based composites [22].

Powder metallurgy is one of the most widely used methods for producing aluminum matrix composites (AMCs) due to its low processing costs and its high versatility[6]. Reinforcement of aluminum alloys (such as 2024, 6061, A356) with ceramic particles or fibers (such as alumina Al_2O_3, SiC or garnet) improve their wear and abrasion resistance. This was investigated in detail by many researchers, and it opens new opportunities for the employment of AMCs in applications where sliding resistance is of concern.

Pramila bai et al [23] observed an increase in wear resistance with increasing SiC particle content from 15 to 25 wt % in an Al-7Si alloy by using a pin-on disk machine.

A more detailed investigation by Alpas and Zhang[14] used a block on ring type apparatus to show that, at low loads, composites reinforced with SiC particles show better wear resistance than the unreinforced Al-7Si alloy.

Wilson et al [24] reported that the addition of Al_2O_3 to the Al6061alloy and SiC to the A356 Al improves their seizure resistances.

Nesarikar et al [25] observed that the friction and wear initially increase and then decrease with increasing load for an aluminum alloy composite reinforced with Al_2O_3 particles in a reciprocating pin-on-plate mode. This reduction was attributed to the increased hardness resulting from the re-embedding of the fractured Al_2O_3 particles near the surface of the composite plate at high loads.

Sharma et al [26] found the wear resistance of Al6061 matrix, garnet particulate reinforced composite to be superior to that of unreinforced matrix alloy.

KÖk and Özdin [27] observed that the reinforcement of 2024 Al matrix alloy with Al_2O_3 particles significantly improves the abrasion wear resistance of the composite

tested against SiC abrasive papers, and the wear resistance of the composite was much higher than that of the unreinforced 2024 aluminum alloy.

Traditionally, brake rotors are manufactured in gray cast iron with a predominantly pearlitic matrix (>95% pearlitic) [28]. It is important to improve the fuel consumption rate by a reduction in the total weight of the vehicle. The break rotor accounts for a large part of the total chassis weight. Aluminum composites with superior thermal conductivity and lower density are harder than the traditional cast iron brake rotors [29]. Therefore, they offer potential for reducing the braking system weight and possibly increasing the wear life of the brake components as well. Therefore, the investigation of the friction and wear behavior of AMCs against friction materials is receiving particular attention.

Although AMC rotors are to be slid against phenolic-based organic/semi-metallic pad materials in practical situations, most of the tribological studies discussed so far on AMCs employ ferrous material as counter bodies. Howell and Ball [30] investigated the dry sliding wear of particulate-reinforced aluminum alloys against automotive friction materials. They found that the specific wear resistance of AMC is higher than that of aluminum alloy and cast iron.

The influence of load and temperature on the dry sliding wear of Al-based composites against friction material was investigated by Straffelini et al. [31]. They found that wear resistance of AMC brake rotors are superior to those of cast iron rotor if the structure and composition of lining material are correctly modified.

Zhang [8] observed that the friction performances and wear resistance for the brake material against the drum with large SiC_p were better than those against the drum with small SiC_p.

Nakanishi et al [7] reported that the higher content of the hard particles on the frictional surface of the brake rotor enhances the heat resistance of the brake rotor. The film formed on the frictional surface of the brake rotor is affected by the ratio of the quantity and the size of the hard particles included in the brake rotor to those of the hard particles included in the brake pad. A higher ratio of the quantity and the size of the hard particles included in the brake pad will destroy the film formed on the frictional surface of rotor.

Shorowordi et al [32] observed that higher sliding velocity leads to lower wear rate and lower friction coefficient for AMCs.

Uyyuru et al [33, 34] found that, when the SiC_p reinforcement in the matrix has wide size distribution, wear rate and friction coefficients are higher compared with a matrix containing mono-size reinforcement. They found that the wear rate increases with the increase in the normal load but it decreases with the increase in the sliding speed. Friction coefficient was found to decrease with the increase in the normal load and the sliding speed.

Natarajan et al [9] compared the wear behavior of AMC sliding against automobile friction material with the conventional grey cast iron at different sliding velocities, loads and sliding distances. The wear of AMC was found to be lower than that of cast iron. However, in all the tests it was observed that the wear of counterface friction material was very high, due to the presence of relatively larger SiC particulates in the AMC.

Incorporation of relatively large ceramic particulates reduces the wear rate of brake rotors, but at the same time it enhances the wear of brake pads. A high wear rate leads to

short replacement intervals for the friction pads, and it thus increases the maintenance costs. Of course, wear of the brake pad is inevitable, but it should be minimized.

The reinforcement used in most of the studies is SiC, which proved to be very expensive. The larger the volume fraction and the finer the size of the reinforcement, the more expensive are the AMCs. Al_2O_3 is characterized by a high level of physical and mechanical properties, e.g. high temperature strength, thermal cyclic resistance, wear resistance and low linear expansion coefficient [35]. Dobrzanski [36] reported that composite materials with Al_2O_3 reinforcing phases increase the tensile properties along with the particles portion in the aluminum matrix growth. Compared to SiC, Al_2O_3 is more stable and has better corrosion and high-temperature behavior [6]. Therefore, the reinforced aluminum by the Al_2O_3 particles has recently become the subject of many studies.

AMCs discussed so far used particulate reinforcement that ranged in diameter from 8 to 43 μm, and most of these reinforcing phases in AMCs form the base material for common cutting tools [37]. Therefore, they cause excessive wear of machine tools during conventional machining processes, such as turning and milling. Developments in AMCs fabrication allowed the use of sub-micron ceramic (Al_2O_3) reinforcement. This improves the economic aspect of the product, since manufacturing is possible with conventional tooling.

Wang et al. [38] observed that the sub-micron Al_2O_3 particle reinforced aluminum matrix composite has larger resistance to the micro-plastic deformation. Longtao et al. [39] reported that, due to the addition of sub-micron Al_2O_3 particles, the hardness of the composite was improved. Al-Qutub et al [40] reported an improvement in wear resistance

with an increasing volume percentage of sub-micron alumina particles in the composite when sliding against ISA4140 steel.

Recent studies show that, when the reinforcement size changes from micro to sub-micro, with the same volume fraction, the amount of reinforcement will be more increased [41]. Due to this volume effect and surface effect, characterization in microstructure and mechanical properties of sub-micron particle reinforced are obviously different from those of micro particle reinforced composite. While most of the studies concentrate only on the composites reinforced by micro-particles, researches on sub-micron particle reinforced composites have not been fully developed. No information is available in the open literature on tribological interactions between sub-micron particle (Al_2O_3) reinforced AMCs and automotive brake pad material, which constitute an important tribological system of great practical interest.

Wear of the rotor and brake material necessitates maintenance. Reducing the size of large ceramic particles to sub-micron in rotor composite would reduce the wear rate of the system and extend the brake component's life. This will extend the service intervals. Therefore, the present study focuses on the friction and wear performance of 6061 Al/Al_2O_3 sub-micron particulate-reinforced composite sliding against the commercial semi-metallic brake material. The semi-metallic friction material has been used in the present investigation, as it has optimal wear resistance and it represents the predominant type of friction materials used in brake industry [42].

CHAPTER 3

EXPERIMENTAL PROCEDURE

3.1 Materials

The materials used in this study are divided into two categories:

1. Automobile brake rotor materials

2. Automobile brake pad material

3.1.1. Rotor materials

(a) AA6061/Al_2O_3/20P:

The material used in the present study is a composite based on a 6061 aluminum alloy metal matrix containing 20% vol. fraction of Al_2O_3 spherical particles with an average size of 0.7 μm processed by powder metallurgy technique. The composite was prepared at Fraunhofer Institut Fetigungstechnik Materialforschung. First, a blend of 6061 aluminum powder (<45 μm) and Al_2O_3 powder (average size = 0.7 μm) was mechanically alloyed in argon atmosphere by using a planetary ball mill for 45 minutes with a rotation speed of 200 rpm. To reduce the welding during the milling, stearic acid was added to the blend at 0.5% of weight.

After producing a homogeneous distribution of Al_2O_3 with the aluminum, the milled powder mixture was cold-isostatically pressed (CIP) to a billet form of about 73 mm diameter, and densified to 80% of the theoretical density . The CIP billet was sintered in inert gas and degassed for several hours prior to the hot extrusion at a temperature of 450°C [43].

(b) Gray Cast Iron:

Traditionally, brake rotors are manufactured from gray cast iron with a predominantly pearlitic matrix. SAE specified J431 G3000 gray cast iron finds application in brake drums, discs and clutch plates to resist thermal shock. Therefore, it was used as the baseline rotor material for comparison with the proposed rotor material.

3.1.2. Brake pad material

A commercial semi-metallic brake pad material was used as the counterface material. It was acquired from SCAN-PAC: 'GREEN GRIPPER' Brake & Clutch Linings, USA. Since these commercial pad materials are proprietary items, their composition is not exactly known. Semi-metallic friction materials offer stable friction, better fade resistance and durability, and rotor compatibility. Detailed specifications of the brake pad material are given below:

Table 3.1: Friction properties of semi-metallic brake pad material [44]

Coefficient of friction (normal)	0.40
Coefficient of friction (hot)	0.38
Wear Rate, (against gray cast iron, SAE J661)	$.004_{max}$ $inch^3$/hp-hr
Friction code	FF
Maximum rubbing speed	10000fpm
Maximum pressure	2000psi
Maximum drum temperature for constant operation	650°F

3.2. Sample preparation

3.2.1 Rotor materials sample

Hollow cylindrical pieces of 12.5mm length, with outer and inner diameters of 24mm and 18mm respectively, were machined from gray cast iron and AA6061/Al_2O_3/20P. These samples were milled to obtain a small pad at one end with an area of 52mm^2. The small pad was milled at only one side to reduce the amount of heat generated at the interface and the normal loading requirements. Both the ends were machined flat. Detail design specifications for these samples are presented in Figure 3.1.

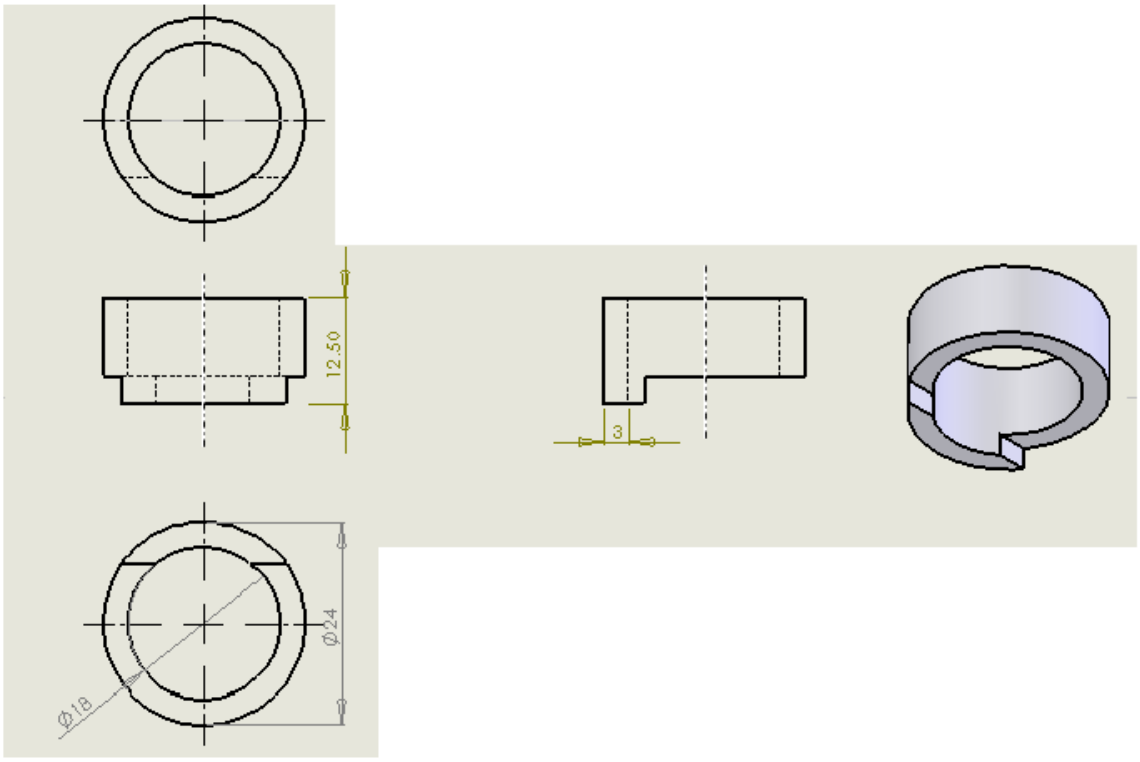

Figure 3.1: Sample design for rotor materials

3.2.2 Brake pad material sample

Brake material was glued into an aluminum cup (Figure 3.2) by using an epoxy adhesive. It was centered and then left for curing for 24 hours. Two holes of 5mm diameter were drilled at the bottom face with a pitch circle diameter of 24mm and depth 10mm. This was done so that the sample fits into the collet without any relative movement. The brake material surface was faced on a lathe machine for alignment with the counter face. The brake pad material with the cup is shown in Figure 3.3.

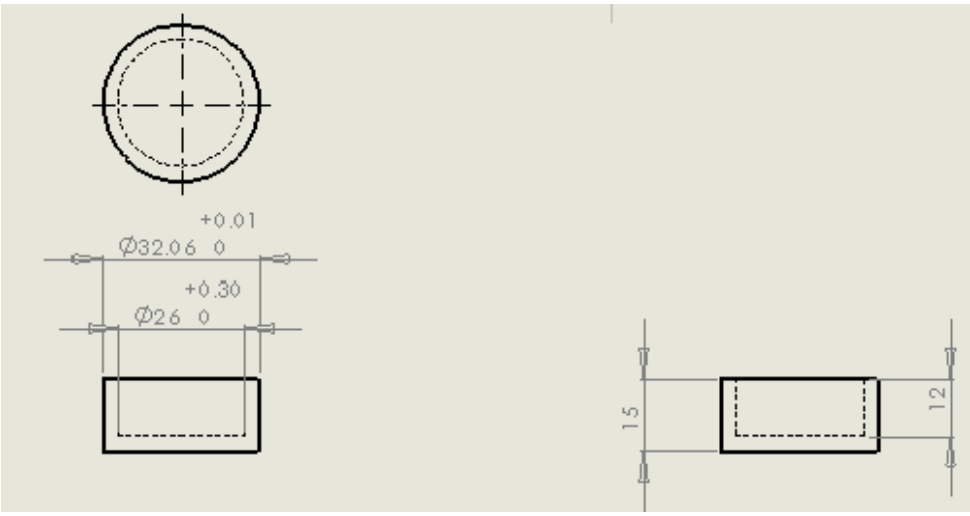

Figure 3.2: Cup design

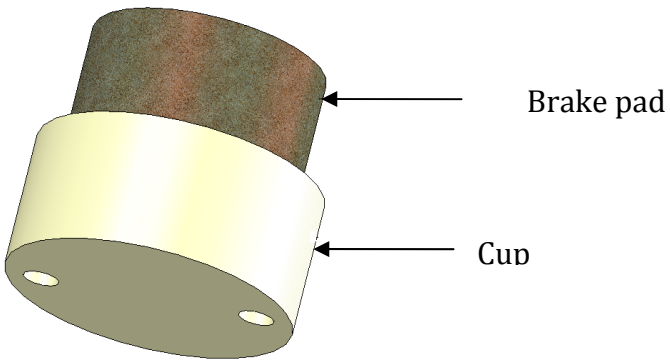

Figure 3.3: Brake pad material sample with cup

3.3. Testing apparatus

Wear tests were conducted at room temperature by using a tribometer available in the mechanical engineering department at King Fahd University of Petroleum and Minerals. The tribometer is a machine which helps to conduct various wear tests providing a controlled and conditioned environment. It characterizes the friction and wear behavior of materials. It serves the tribologically oriented development of materials and lubricants through proper evaluation of tribological behavior, especially wear and friction. The present tribometer can simulate wear for the specified speed, time, temperature and sliding distance. It can measure the friction coefficient as well as sense the temperature. This tribometer has the following specifications:

- Normal load application from 0.5 N to 500 N.
- Continuous bidirectional rotation of disc over a large range of sliding velocities (35 to 6700 rpm).
- Oscillations over a range of amplitudes simulative of bearings and seals in reciprocating machinery.
- High temperature capability (upto 500°±5°C).
- Torque measurements ±10N-m maximum with an accuracy of 0.025N-m.
- Dry and lubricated test capability.
- Controlled gas environment non-reactant with stainless steel or tool steel.
- Six point temperature measurement capability with an accuracy of ±0.5°C.

A view of this tribometer is shown in Figure 3.4.

Figure 3.4: High temperature tribometer

3.4 Experimental setup

Figure 3.5 shows the pad-on-disk configuration designed for the tribometer. A rotor material sample with a pad-like projection is held in a collet which grips on the upper shaft. This shaft remains non-rotating. A brake material sample with a disk-like flat surface is held in a collet which grips on the lower shaft (rotating shaft). In this case, the brake pad material slides against the rotor material. The upper and lower shafts are concentric and aligned to ±0.025mm according to tribometer specifications.

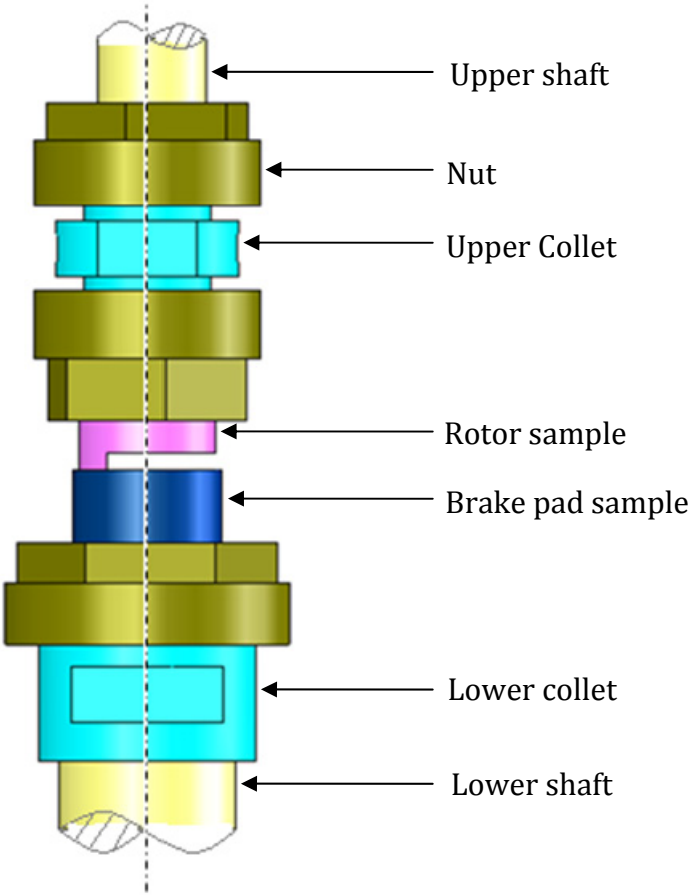

Figure 3.5 Pad-on-disk experimental setup

An attempt was made to machine the brake material in order to make it into a pad. It started shearing and cracking, because it was not held under compression during machining (as it has good compression strength). Eventually, a fixture was designed and manufactured to hold it under compression during machining. Since there is a taper in all the brake material pieces, it could not be used. The researcher decided not to machine the brake material but to use it as received. Therefore, the brake pad material was used as a disk and the rotor material was used to make a pad in a typical pad-on-disk configuration.

3.5 Testing procedures

3.5.1 Microstructural examination

A metallographic sample was cut from the bar of AA6061/Al_2O_3/20P composite and gray cast iron in the form of circular discs. Samples were ground by using SiC abrasive paper with increasing grit sizes of 320, 400 and 600. The samples were then polished on micro-cloth with progressively finer grades of diamond paste. The polished surface of AA6061/Al_2O_3/20P was etched by using Keller's reagent, and that of gray cast iron with Nital reagent. JEOL scanning electron microscope (JSM-6460LV) was used to examine the microstructure of AA6061/Al_2O_3/20P composite. The microstructure of gray cast iron was examined by using an optical microscope (Zeiss axioplan2 imaging universal microscope).

3.5.2 Microhardness test

The Buehler Vickers microhardness testing machine (Type 1600-6306) was used to perform microhardness tests on a sample of AA6061/Al_2O_3/20P composite as well as a gray cast iron sample. Hardness was measured at three locations on each sample surface. The average reading from the three samples was reported.

3.5.3 Density measurement and uncertainty analysis

The density of the samples was calculated by using the following relationship,

$$\rho = \frac{m}{V} \tag{1}$$

where ‘m’ is the sample mass and ‘V’ is the sample volume using the following equation

$$V = \frac{\pi}{4} d^2 l \tag{2}$$

where

d is the sample diameter and

l is the length

Uncertainty in the density of brake material and of gray cast iron material was determined by using the data reduction equation.

$$\rho = \frac{4m}{\pi d^2 l} \tag{3}$$

Where *m, d* and *l* are measured variables. Since they are measured by using the same instrument (Starret electronic digital caliper, model number 721A), bias errors in *d* and *l* are fully correlated. The uncertainty analysis expression that must be used for determining bias Bρ is given as

$$B_\rho = \left[\left(\frac{\partial \rho}{\partial m} \right)^2 B_m{}^2 + \left(\frac{\partial \rho}{\partial d} \right)^2 B_d{}^2 + \left(\frac{\partial \rho}{\partial l} \right)^2 B_l{}^2 + 2 \left(\frac{\partial \rho}{\partial d} \right) \left(\frac{\partial \rho}{\partial l} \right) B_d B_l \right]^{1/2} \tag{4}$$

Divide the general expression (4) by the density ρ, and recast it into the form

$$\frac{B_\rho}{\rho} = \left[\left(\frac{1}{\rho} \frac{\partial \rho}{\partial m} \right)^2 B_m{}^2 + \left(\frac{1}{\rho} \frac{\partial \rho}{\partial d} \right)^2 B_d{}^2 + \left(\frac{1}{\rho} \frac{\partial \rho}{\partial l} \right)^2 B_l{}^2 + 2 \left(\frac{1}{\rho} \frac{\partial \rho}{\partial d} \right) \left(\frac{1}{\rho} \frac{\partial \rho}{\partial l} \right) B_d B_l \right]^{1/2} \tag{5}$$

The above expression is simplified by substituting the partial derivatives,

$$\frac{B_\rho}{\rho}=\left[\left(\frac{B_m}{m}\right)^2+\left(\frac{-2}{d}B_d\right)^2+\left(-\frac{1}{l}B_l\right)^2+2\left(\frac{-2}{d}\right)\left(\frac{-1}{l}\right)B_dB_l\right]^{1/2} \quad (6)$$

The uncertainty analysis expression which must be used for determining precision Pρ in density is given by

$$\frac{P_\rho}{\rho}=\left[\left(\frac{1}{\rho}\frac{\partial\rho}{\partial m}\right)^2 P_m{}^2+\left(\frac{1}{\rho}\frac{\partial\rho}{\partial d}\right)^2 P_d{}^2+\left(\frac{1}{\rho}\frac{\partial\rho}{\partial l}\right)^2 P_l^2\right]^{1/2} \quad (7)$$

Substituting for partial derivatives,

$$\frac{P_\rho}{\rho}=\left[\left(\frac{1}{m}P_m\right)^2+\left(\frac{-2}{d}P_d\right)^2+\left(\frac{-1}{l}P_l\right)^2\right]^{1/2} \quad (8)$$

3.5.3.1. Uncertainty analysis for density of gray cast iron

(a) <u>Zeroth Order Replication Level Analysis</u>

Table 3.2: Zeroth-order estimates of the bias and precision limits for variables in density value determination.

Variable	Bias Limit	Precision Limit
m	±0.1 *mg*	± 0.05 *mg*
l	±0.03 *mm*	±0.005 *mm*
d	±0.03 *mm*	±0.005 *mm*

Table 3.3: Nominal values from wear test

Measured Variable	Value
m	7.81333 *gm*
l	9.50 *mm*
d	12.08 *mm*
ρ	0.007182265 gm/mm^3

The bias expression limit in the result can be determined by substituting the nominal values from Table 3.3 with the bias and precision limit estimates in Table 3.2 in equation 6. The bias limit in the result becomes

$$B_\rho = \pm 5.835 \text{ X } 10^{-5} \text{ gm/mm}^3 \quad (9)$$

And the precision is

$$P_\rho = \pm 7.046 \text{ X } 10^{-6} \text{ gm/mm}^3 \quad (10)$$

The uncertainty with 95% coverage in the density value determination is found by the equation 11,

$$U_\rho = \left[B_\rho^{\,2} + P_\rho^{\,2} \right]^{1/2} \quad (11)$$

$$U_\rho = \left[\left(5.835 \times 10^{-5}\right)^2 + \left(7.046 \times 10^{-6}\right)^2 \right]^{1/2} = 5.88 \times 10^{-5}\, gm/mm^3 \quad (12)$$

Therefore, the density of a single sample of gray cast iron can be measured with an uncertainty of 0.82%.

(b) First Order Replication Level Analysis:

The density value of five samples was determined. The density results are summarized in Table 3.4.

Table 3.4: Density values for gray cast iron samples

Sample Number	Density Value (gm / mm^3)
1	0.00718
2	0.00723
3	0.00717
4	0.00729
5	0.00725

The mean density value is

$$\bar{\rho} = 0.007227 \ gm / mm^3 \tag{13}$$

The precision index of the collection of five results is

$$\hat{S}_{\rho} = 4.98\text{x}10^{-5} \ gm / mm^3 \tag{14}$$

For the five data points, the value of t is 2.776, and so

$$P_{\bar{\rho}} = \pm t \ \hat{S}_{\rho}$$

$$= 1.385\text{x}10^{-4} \ gm / mm^3 \tag{15}$$

The precision limit in the equation 15 represents the range around the mean value at which the density value determination for another sample would fall with 95% confidence.

The precision limit due to sample-to-sample variation in the gray cast iron composition is found from 1st order and zeroth order precision limits as

$$\left(p_{\rho}\right)_{mat} = \left[\left(p_{\rho}\right)^2_{1st} - \left(p_{\rho}\right)^2_{zeroth}\right]^{1/2} \tag{16}$$

$$= \left[\left(1.385\times10^{-4}\right)^2 - \left(7.046\times10^{-6}\right)^2 \right]^{1/2}$$

$$= \pm\ 1.383\text{x}10^{-4}\ gm/mm^3 \tag{17}$$

(c) Nth-Order Replication Level Analysis

The average density of five samples was found to be $0.007227\ gm/mm^3$. The uncertainty in this average result is

$$U_\rho = \left[B_\rho{}^2 + P_\rho{}^2 \right]^{1/2} \tag{18}$$

where

$$P_\rho = \text{t Sρ} \tag{19}$$

$$S_\rho = \frac{\hat{S}_\rho}{\sqrt{M}} \tag{20}$$

Substituting for $\hat{S}_\rho$ from equation 14 to obtain

$$\hat{S}_\rho = \frac{4.98903\text{x}10^{-5}}{\sqrt{5}}\ gm/mm^3$$
$$P_{\bar{\rho}} = \frac{(2.776)\times(4.98903\text{x}10^{-5})}{\sqrt{5}} = 6.1937\times10^{-5}\ gm/mm^3 \tag{21}$$

and

$$U_{\rho^-} = \left[\left(5.835\times10^{-5}\right)^2 + \left(6.1937\times10^{-5}\right)^2 \right]^{1/2} = 8.5\times10^{-5}\ gm/mm^3 \tag{22}$$

Therefore, the average density value with 95% coverage is

$$7.227218\times10^{-3}\pm8.5\times10^{-5}\ gm/mm^3 \quad (23)$$

3.5.3.2. Uncertainty analysis for density of brake material:

Model discussed in section 3.1 is adopted.

(a) Zeroth-order replication level analysis:

Bias limit, $B_\rho = \pm 1.25$ X 10^{-5} gm/mm^3 (24)

Precision limit, $P_\rho = \pm 2.08$ X 10^{-6} gm/mm^3 (25)

The uncertainty (with 95% coverage) in the density value determination of a single sample is

U_ρ = 1.267 X 10^{-5} gm/mm^3 (26)

Therefore, the density of a single sample of brake material can be measured with an uncertainty of 0.36%.

(b) First order replication level analysis:

The precision limit due to sample-to-sample variation in brake material composition is found to be $\left(P_\rho\right)_{mat}$ = 1.52 X 10^{-4} gm/mm^3 (27)

(c) N-th order replication level analysis:

Average density, ρ=0.00345 gm/mm^3 (28)

Uncertainty in average density, U_ρ =7.7x10^{-5} gm/mm^3 (29)

Therefore, average density value with 95% coverage is,

$$3.45\times10^{-3} \pm 7.7\times10^{-5}\ gm/mm^3 \quad (30)$$

3.5.3.3 Uncertainty analysis for density of 20% VF-Al/Al$_2$0$_3$ composite

Model discussed in section 3.1 is adopted.

(a) Zeroth-order replication level analysis:

Bias limit, $B\rho = \pm 8.37X10^{-6}\ gm/mm^3$ (31)

Precision limit, $P\rho = \pm 7.65X10^{-6}\ gm/mm^3$ (32)

The uncertainty (with 95% coverage) in the density value determination of a single sample is

$U\rho = 1.14x10^{-5}\ gm/mm^3$ (33)

Therefore, the density of a single sample of the aluminum composite can be measured with an uncertainty of 0.39%.

(b) First-order replication level analysis:

The precision limit due to sample-to-sample variation in composite material composition is found to be

$$\left(P_\rho\right)_{mat} = 3.8\ X\ 10^{-5}\ gm/mm^3 \quad (34)$$

(c) Nth-order replication level analysis:

Average density,

$\rho=2.8865x10^{-3}\ gm/mm^3$ (35)

The theoretical density value for aluminium composite is $3.7x10^{-3}$ gm/mm^3. The average density is 78% of the theoretical density. This is in close agreement with the material specifications for density. The homogeneous milled powder mixture of Al_2O_3 with the aluminum was cold-isostatically pressed (CIP) to a billet form densified to 80% of the theoretical density [43].

Uncertainty in average density,

$U\rho = \pm 1.8x10^{-5}\ gm/mm^3$ (36)

Therefore,

average density value with 95% coverage is $2.8868\times10^{-3} \pm 1.8\times10^{-5}\ gm/mm^3$ (37)

3.5.4 Calibration

(a) Disc Speed Calibration

The spindle carrying the disc is rotated by a variable speed motor driven by Eurotherm 150 HP AC Drive with an output frequency range of 0 to 240 Hz. The rotational speed N is calibrated by using a Hampden digital tachometer (model HPT-100A). It measures rotational speeds between 50rpm and 10,000 rpm, and it is accurate within 1rpm. The disc is rotated by a variable speed motor connected to the spindle by a synchronous toothed belt. The motor shaft can be attached with three gears with different numbers of teeth i.e. 40, 46 and 14. These gears can be connected to the gear (20 teeth) on the disc spindle by means of the synchronous toothed belt. These gear drives provide three gear

ratios of 2.3:1, 2:1, and 0.7:1. For speed calibration, the input frequency in Hertz was varied in the AC drive from 0 to 60Hz, and the output rpm N of the spindle carrying the disc was recorded by using a tachometer. These tests were repeated three times, and the average rpm value was considered and plotted. The relation between speed and frequency are presented in Table 3.5 and Figure 3.6.

Table: 3.5 Disc speed calibration for gear ratio 0.7:1

Hertz	**rpm1**	**rpm2**	**rpm3**	**Average rpm**
10	413	413	413	413
15	621	621	621	621
20	828	828	828	828
25	1035	1035.5	1035	1035.167
30	1242	1242.5	1242	1242.167
35	1449.5	1450	1449.5	1449.667
40	1656	1656	1656	1656
45	1863	1863	1863	1863
50	2071	2071	2071	2071
55	2279.5	2280	2279.5	2279.667
60	2489	2489	2489	2489

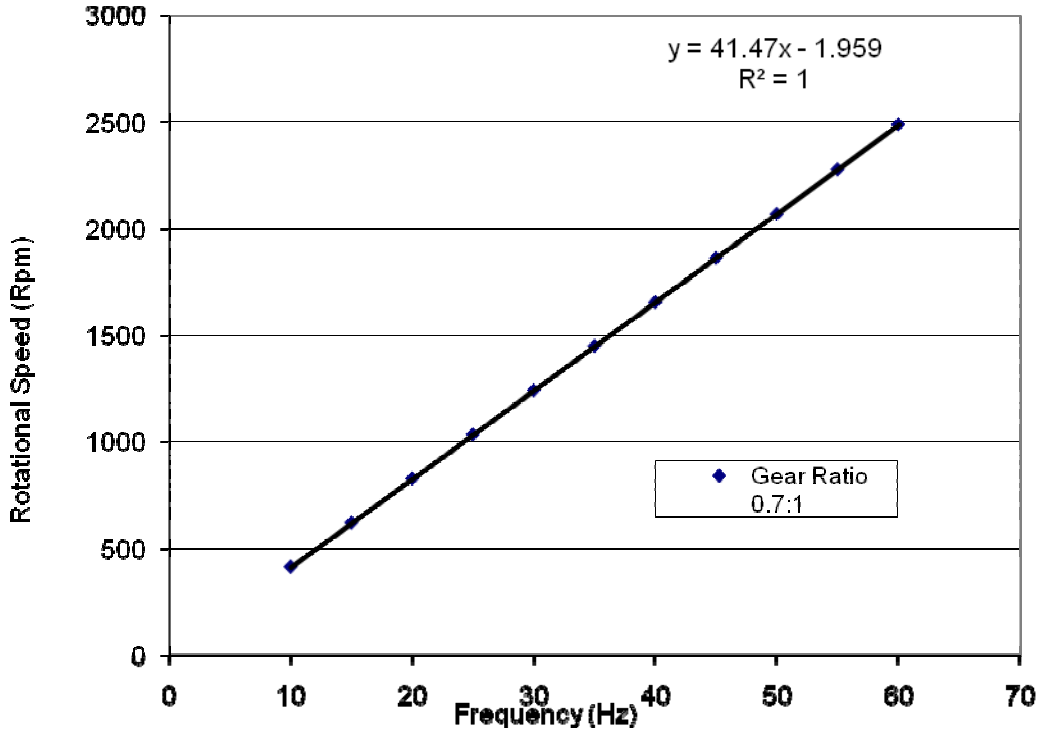

Figure 3.6 Disc speed variation with input frequency at gear ratio 0.7

(b) Friction Recorder Calibration

The zero friction coefficient position of the pointer on the recorder at zero frictional force can be fixed by adjusting the pointer at zero load. First calculate the calibration load (F_C), based on the expected value of the co-efficient of friction (μ) at the actual experiment load (P). Then apply this calculated load on the specimen (pin) in the direction of the frictional force, and adjust the output recorder to calibrate it within its range.

Let:

P= actual test load

F_N= normal reaction at contact point at test load

F_C= load to be used for calibration=load sensed by the load cell

F_μ= frictional force that would be acting at the contact point

μ= co-efficient of friction at test load

r = distance of point of frictional contact between ring and disc from shaft axis

From Figure 3.7,

the normal reaction will be equal to the test load, i.e. $\mathbf{F_N = P}$ (1)

and the frictional force acting at the contact point will be $\mathbf{F_\mu = \mu F_N}$ (2)

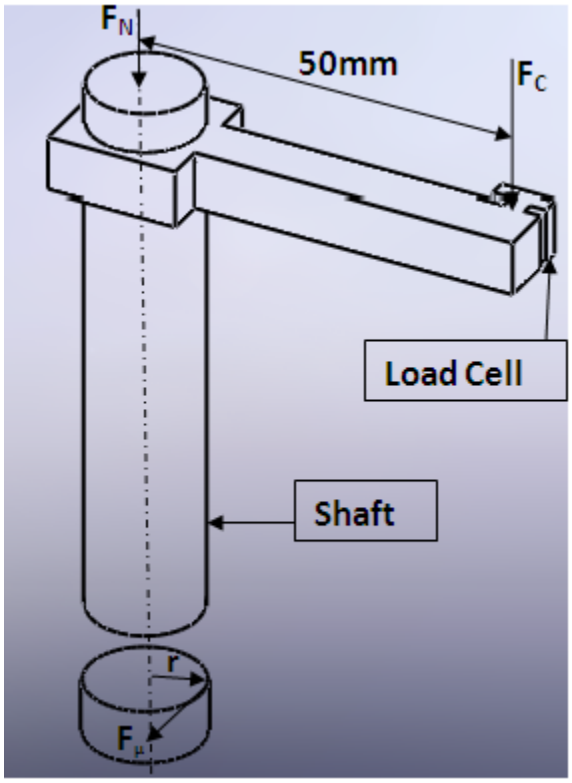

Figure 3.7. Calibration load calculation

As the load cell reads the frictional force F_μ, the value of the calibration load F_C is calculated by balancing the torque acting on the shaft axis.

$$F_\mu \times r = F_C \times 50$$

$$F_\mu = \frac{50F_C}{r} \quad (3)$$

From equation 2,

$$F_C = \frac{\mu F_N r}{50} \quad (4)$$

Since r =10.5mm,

$$F_c = 0.21\mu F_N \quad (5)$$

3.5.5. Wear testing

- **First Stage**: The ring surface was made flat to support the load over its entire cross-section. This was achieved by running the test for 500 seconds with small loads and at low speeds on A320 emery paper fixed over a flat surface.
- **Second stage**: At the beginning of the wear test, under the actual load and speed conditions, the contact area and nature of contact may change. Hence, every test was started with a run-in-wear stage. Both the rotor and the brake pad material were pre-run against each other for 200 seconds. This stage minimizes or avoids initial turbulence associated with the initial part of the friction and wear curve.
- **Third Stage:** The final stage is the actual testing. The ring materials were cleaned with acetone prior to testing in order to prevent any transfer of contaminations before each test. The brake materials were not cleaned with solvents, owing to the problems of porosity and the potential for penetration and attack of the phenolic binder material by the acetone. They were only dusted off with a blast of dry air. Weight losses of the ring and disk were measured by using a high precision

electronic balance (Shimadzu's AUW220D dual range semi-micro balance). The rotor material samples were held in a collet that grips the upper shaft. The brake material sample was held in a collet that grips the lower shaft. The required load was applied on the sample in the normal direction through the upper shaft. The direction of disc rotation, the motor speed and the test duration were set through the control panel of the tribometer. The wear tests were conducted at varying loads and sliding speeds. All tests were performed under dry sliding conditions. At each data point, tests were repeated thrice, and the average value with the standard error of mean was reported. Each test was run for 500m at a given load, during which the evolution of the contact temperature was recorded by placing the K-type thermocouple 2mm above the contact surface. To determine the coefficient of friction, an XY recorder was connected to the tribometer's torque measuring instrument, and calibrated by using standard loads. The samples were removed after the conclusion of time. The rotor material sample was cleaned with acetone, and the brake pad material was dusted off with a blast of air. They were weighed again to determine the mass loss. The volume loss was calculated by using the density of the composite according to the following equation:

$$\Delta V = \frac{\Delta m}{\rho}$$

where m is the mass and ρ is the density of the sample**.** The experimental matrix is shown in the Table 3.6. By keeping a constant load, the experiment was performed at varying sliding velocities.

Table: 3.6 Experiment matrix

	1 MPa	2 MPa	3 MPa
1m/s	1 MPa-m/s	2 MPa-m/s	3 MPa-m/s
1.5m/s	1.5 MPa-m/s	3 MPa-m/s	4.5 MPa-m/s
2m/s	2 MPa-m/s	4 MPa-m/s	6 MPa-m/s
2.5m/s	2.5 MPa-m/s	5 MPa-m/s	7.5 MPa-m/s

3.5.6 Wear rate uncertainty analysis

Wear rate is defined as the volume loss per unit sliding distance. Therefore, wear rate (w) can be expressed as:

$$w = \frac{\Delta V}{S} = \frac{\Delta V}{vt} \tag{1}$$

where,

$$\text{Volume loss, } \Delta V = \frac{\Delta m}{\rho} = \frac{(m_1 - m_2)}{\rho} \tag{2}$$

$$\text{Sliding velocity, } v = \frac{2\Pi R\text{N}}{60} \tag{3}$$

$$\text{Density, } \rho = \frac{\pi d^2 l}{4} \tag{4}$$

(Δm is the mass change in the sample due to wear, ρ is the sample density, m_1 initial mass of the sample, m_2 final mass of the sample, R is the wear track radius, N is the number of rpm, t is the time for test run, d is the sample diameter*,* l is the sample length).

Therefore, the above equation changes to,

$$w = \frac{120\left(m_1 - m_2\right) d^2 l}{RNmt} \tag{5}$$

Uncertainty in time (t) is assumed negligible. Hence, the data reduction equation (DRE),

$$\text{w= f } (m_1,\ m_2,\ d,\ l,\ R,\ N,\ m) \tag{6}$$

For measurements of wear rate, the measurand is not observed directly, but it is determined from measurements of the individual input quantities $m_1,\ m_2,\ d,\ l,\ R,\ N,\ m$. Since, the same instrument is used to measure $R,\ l,$ and d; there is a correlation between them. The uncertainty analysis expression which is used for determining bias B_w is given as:

$$\begin{aligned}
\left(B_w\right)^2 = &\left(\frac{\partial w}{\partial m_1}\right)^2 B_{m_1}^2 + \left(\frac{\partial w}{\partial m_2}\right)^2 B_{m_2}^2 + 2\left(\frac{\partial w}{\partial m_1}\right)\left(\frac{\partial w}{\partial m_2}\right) B_{m_1} B_{m_2} + \left(\frac{\partial w}{\partial d}\right)^2 B_d^2 \\
&+ \left(\frac{\partial w}{\partial l}\right)^2 B_l^2 + \left(\frac{\partial w}{\partial R}\right)^2 B_R^2 + 2\left(\frac{\partial w}{\partial d}\right)\left(\frac{\partial w}{\partial l}\right) B_d B_l + 2\left(\frac{\partial w}{\partial l}\right)\left(\frac{\partial w}{\partial R}\right) B_l B_R \\
&+ 2\left(\frac{\partial w}{\partial R}\right)\left(\frac{\partial w}{\partial d}\right) B_R B_d + \left(\frac{\partial w}{\partial N}\right)^2 B_N^2 + \left(\frac{\partial w}{\partial m}\right)^2 B_m^2 \\
&+ 2\left(\frac{\partial w}{\partial m}\right)\left(\frac{\partial w}{\partial m_1}\right) B_m B_{m_1} + 2\left(\frac{\partial w}{\partial m}\right)\left(\frac{\partial w}{\partial m_2}\right) B_m B_{m_2}
\end{aligned} \tag{7}$$

Dividing the equation by the square of the experimental result, the equation simplifies as:

$$\left(\frac{B_w}{w}\right)^2 = \left(\frac{1}{w}\frac{\partial w}{\partial m_1}\right)^2 B_{m_1}^2 + \left(\frac{1}{w}\frac{\partial w}{\partial m_2}\right)^2 B_{m_2}^2 + 2\left(\frac{1}{w}\frac{\partial w}{\partial m_1}\right)\left(\frac{1}{w}\frac{\partial w}{\partial m_2}\right) B_{m_1} B_{m_2}$$
$$+\left(\frac{1}{w}\frac{\partial w}{\partial d}\right)^2 B_d^2 + \left(\frac{1}{w}\frac{\partial w}{\partial l}\right)^2 B_l^2 + \left(\frac{1}{w}\frac{\partial w}{\partial R}\right)^2 B_R^2 + 2\left(\frac{1}{w}\frac{\partial w}{\partial d}\right)\left(\frac{1}{w}\frac{\partial w}{\partial l}\right) B_d B_l$$
$$+2\left(\frac{1}{w}\frac{\partial w}{\partial l}\right)\left(\frac{\partial w}{\partial R}\right) B_l B_R + 2\left(\frac{1}{w}\frac{\partial w}{\partial R}\right)\left(\frac{1}{w}\frac{\partial w}{\partial d}\right) B_R B_d + \left(\frac{1}{w}\frac{\partial w}{\partial N}\right)^2 B_N^2$$
$$+\left(\frac{1}{w}\frac{\partial w}{\partial m}\right)^2 B_m^2 + 2\left(\frac{1}{w}\frac{\partial w}{\partial m}\right)\left(\frac{1}{w}\frac{\partial w}{\partial m_1}\right) B_m B_{m_1} + 2\left(\frac{1}{w}\frac{\partial w}{\partial m}\right)\left(\frac{1}{w}\frac{\partial w}{\partial m_2}\right) B_m B_{m_2} \quad (8)$$

The above expression is simplified by substituting the partial derivatives. Bias in m_1 and m_2 cancels out due to correlation between them. Also, the correlated bias in m with m_1 and m_2 gets cancelled out.

$$\left(\frac{B_w}{w}\right)^2 = \left(\frac{2}{d}B_d\right)^2 + \left(\frac{1}{l}B_l\right)^2 + \left(\frac{1}{R}B_R\right)^2 + \left(\frac{4}{ld}\right) B_d B_l - \left(\frac{4}{Rd}\right) B_d B_R - \left(\frac{2}{lR}\right) B_l B_R$$
$$+\left(\frac{1}{N}B_N\right)^2 + \left(\frac{1}{m}B_m\right)^2 \quad (9)$$

The uncertainty analysis expression which is used for determining precision, P_w in wear rate is given by

$$P_w^2 = \left(\frac{\partial w}{\partial m_1}\right)^2 P_{m_1}^2 + \left(\frac{\partial w}{\partial m_2}\right)^2 P_{m_2}^2 + \left(\frac{\partial w}{\partial d}\right)^2 P_d^2 + \left(\frac{\partial w}{\partial l}\right)^2 P_l^2 + \left(\frac{\partial w}{\partial R}\right)^2 P_R^2$$
$$+\left(\frac{\partial w}{\partial N}\right)^2 P_N^2 + \left(\frac{\partial w}{\partial m}\right)^2 P_m^2 \quad (10)$$

Dividing the equation by the square of the experimental result, the equation simplifies as

$$\left(\frac{P_w}{w}\right)^2 = \left(\frac{1}{w}\frac{\partial w}{\partial m_1}\right)^2 P_{m_1}^2 + \left(\frac{1}{w}\frac{\partial w}{\partial m_2}\right)^2 P_{m_2}^2 + \left(\frac{1}{w}\frac{\partial w}{\partial d}\right)^2 P_d^2 + \left(\frac{1}{w}\frac{\partial w}{\partial l}\right)^2 P_l^2 + \left(\frac{1}{w}\frac{\partial w}{\partial R}\right)^2 P_R^2 + \left(\frac{1}{w}\frac{\partial w}{\partial N}\right)^2 P_N^2 + \left(\frac{1}{w}\frac{\partial w}{\partial m}\right)^2 P_m^2 \quad (11)$$

The above expression is simplified by substituting the partial derivatives,

$$\left(\frac{P_w}{w}\right)^2 = \left(\frac{1}{m_1 - m_2}P_{m_1}\right)^2 + \left(\frac{-1}{m_1 - m_2}P_{m_2}\right)^2 + \left(\frac{2}{d}P_d\right)^2 + \left(\frac{1}{l}P_l\right)^2 + \left(\frac{-1}{R}P_R\right)^2 + \left(\frac{-1}{m}P_m\right)^2 \quad (12)$$

In the following sections, we detail our evaluations of the standard uncertainties for the input quantities Δm, N, R and ρ.

(a) Standard Uncertainty in m_1, m_2, and m.

These values were recorded by using a Shimadzu AUW220D dual range semi-micro balance. The scale has a resolution of 0.1mg for a range of 220 g and a resolution of 0.01mg for a range of 82g. The device has inbuilt software for auto calibration. The device has a linearity of ±0.2mg for a range of 220 g and a linearity of ±0.1mg for a range of 82g. A linearity of ±0.1mg is used as bias. The manufacturer's data sheet lists a repeatability of 0.1mg for a large range and a repeatability of 0.05mg for a small range. A repeatability of 0.05mg is used for precision, $P(m_i) = 0.05mg$.

(b) Standard uncertainty in N (rpm)

The lower spindle of the tribometer was rotated by a variable speed motor driven by the Eurotherm 150 HP AC Drive with an output frequency range of 0-240 Hz. The

gear ratio used was 0.7:1. The rotational speed N was calibrated by using a Hampden digital tachometer (model HPT-100A). It measures the rotational speeds between 50 rpm and 10,000 rpm, and it is accurate within 1 rpm. Therefore, the calibration standard accuracy was assigned to the rpm measurement at each data point. The input frequency in Hertz was varied in the AC drive from 0-60Hz, and the output rpm (N) of the spindle was recorded by using a tachometer. The regression fit with the equation was developed by using Excel as shown in Figure 3.6. The uncertainty in using the corresponding fit (= √ (residual error/n-2)) was evaluated by using the regression analysis. It turned out to be 13 rpm. This is a fossilized bias. The standard bias value for the speed of 13 rpm was obtained by combining the two sources of bias.

(c) Standard uncertainty in *R, l,* and *d*

The wear track radius was fixed in the set up. It is the centre-to-centre horizontal distance between shaft and pad. The pad holder is designed to accommodate this distance. The track radius was measured by using a Starret electronic digital caliper (model number 721A). The manufacturer's specification for the instrument accuracy is 0.03 mm. So, the bias $B(R)$ is assumed to be 0.03mm. The instrument has a resolution of 0.01 mm. The precision limit P(R) for radius measurement was estimated to be ±0.005mm. The same bias and precision limits were used for length and diameter of the sample.

3.5.6.1 Overall uncertainty

Substituting these values in equations 9 and 12, the bias and precision limits typical for gray cast iron sliding against brake material at 1m/s and 1MPa are obtained as follows:

Table: 3.7 Bias and precision limits of variables and nominal values

Variable	Bias limit	Precision limit	Nominal value
m1	±0.1*mg*	±0.05*mg*	12.91243*gm*
m2	±0.1*mg*	±0.05*mg*	12.90663*gm*
d	±0.03*mm*	±0.005*mm*	12*mm*
l	±0.03*mm*	±0.005*mm*	9.838*mm*
R	±0.03*mm*	±0.005*mm*	10.5*mm*
N	±13*rpm*	0	910*rpm*
m	±0.1*mg*	±0.05*mg*	8.1116*gm*

$$\left(\frac{B_w}{w}\right)^2 = 2.3\times10^{-4} \tag{12}$$

$$\left(\frac{P_w}{w}\right)^2 = 1.5\times10^{-4} \tag{13}$$

The combined standard uncertainty for wear rate is calculated by using equation 15. Table 3.7 summarizes the nominal values, bias and precision limits.

$$\left(\frac{U_w}{w}\right)^2 = \left(\frac{B_w}{w}\right)^2 + \left(\frac{p_w}{w}\right)^2$$
$$= 3.8\times10^{-4} \quad (15)$$

$$\left(\frac{U_w}{w}\right) = 0.0195 = 1.9\% \quad (16)$$

Therefore, the uncertainty in measuring the wear rate is 1.9%.

The precision limit due to sample-to-sample variation in gray cast iron composition is found to be $\left(P_w\right)_{mat}$ = 0.075 mm^3/km (17)

Average wear rate, $\bar{w}$ = 1.514 mm^3/km (18)

Uncertainty in average wear rate, $U_{\bar{w}}$ = 0.425 mm^3/km (19)

Therefore, the average wear rate value with 95% coverage is,

$$1.514 \pm 0.425 mm^3 / km \quad (20)$$

3.5.7 Friction coefficient uncertainty analysis

The coefficient of friction is calculated by using the following relationship,

$$\mu = \frac{F_C L_C}{F_N R} \quad (1)$$

(F_C- Calibration load, F_N- Normal reaction, L_C- load cell distance from shaft axis, R- Wear track radius)

Hence, the data reduction equation (DRE)

$$\mu = f\left(F_C, F_N, L_C, R\right) \tag{2}$$

The uncertainty analysis expression which is used for determining bias B_μ is given as:

$$\begin{aligned}\left(B_\mu\right)^2 = &\left(\frac{\partial \mu}{\partial F_C}\right)^2 B^2{}_{F_C} + \left(\frac{\partial \mu}{\partial F_N}\right)^2 B^2{}_{F_N} + 2\left(\frac{\partial \mu}{\partial F_C}\right)\left(\frac{\partial \mu}{\partial F_N}\right) B_{F_C} B_{F_N} + \left(\frac{\partial \mu}{\partial L_C}\right)^2 B^2{}_{L_C} \\ &+ \left(\frac{\partial \mu}{\partial R}\right)^2 B^2{}_R + 2\left(\frac{\partial \mu}{\partial L_C}\right)\left(\frac{\partial \mu}{\partial R}\right) B_{L_C} B_R\end{aligned} \tag{3}$$

Dividing the equation by the square of the experimental result, the equation simplifies as:

$$\begin{aligned}\left(\frac{B_\mu}{\mu}\right)^2 = &\left(\frac{1}{\mu}\frac{\partial \mu}{\partial F_C}\right)^2 B^2{}_{F_C} + \left(\frac{1}{\mu}\frac{\partial \mu}{\partial F_N}\right)^2 B^2{}_{F_N} + 2\left(\frac{1}{\mu}\frac{\partial \mu}{\partial F_C}\right)\left(\frac{1}{\mu}\frac{\partial \mu}{\partial F_N}\right) B_{F_C} B_{F_N} \\ &+ \left(\frac{1}{\mu}\frac{\partial \mu}{\partial L_C}\right)^2 B^2{}_{L_C} + \left(\frac{1}{\mu}\frac{\partial \mu}{\partial R}\right)^2 B^2{}_R + 2\left(\frac{1}{\mu}\frac{\partial \mu}{\partial L_C}\right)\left(\frac{1}{\mu}\frac{\partial \mu}{\partial R}\right) B_{L_C} B_R\end{aligned} \tag{4}$$

The expression is simplified by substituting the partial derivatives as follows:

$$\begin{aligned}\left(\frac{B_\mu}{\mu}\right)^2 = &\left(\frac{B_{F_C}}{F_C}\right)^2 + \left(\frac{B_{F_N}}{F_N}\right)^2 - 2\left(\frac{B_{F_C}}{F_C}\right)\left(\frac{B_{F_N}}{F_N}\right) + \left(\frac{B_{L_C}}{L_C}\right)^2 \\ &+ \left(\frac{B_R}{R}\right)^2 - 2\left(\frac{B_{L_C}}{L_C}\right)\left(\frac{B_R}{R}\right) B_{L_C} B_R\end{aligned} \tag{5}$$

The uncertainty analysis expression which is used for determining precision P_μ in friction coefficient is given by

$$\left(P_\mu\right)^2 = \left(\frac{\partial \mu}{\partial F_C}\right)^2 P^2{}_{F_C} + \left(\frac{\partial \mu}{\partial F_N}\right)^2 P^2{}_{F_N} + \left(\frac{\partial \mu}{\partial L_C}\right)^2 P^2{}_{L_C} + \left(\frac{\partial \mu}{\partial R}\right)^2 P^2{}_R \tag{6}$$

Dividing the equation by the square of the experimental result, the equation simplifies as:

$$\left(\frac{P_\mu}{\mu}\right)^2 = \left(\frac{1}{\mu}\frac{\partial\mu}{\partial F_C}\right)^2 P^2{}_{F_C} + \left(\frac{1}{\mu}\frac{\partial\mu}{\partial F_N}\right)^2 P^2{}_{F_N} + \left(\frac{1}{\mu}\frac{\partial\mu}{\partial L_C}\right)^2 P^2{}_{L_C} + \left(\frac{1}{\mu}\frac{\partial\mu}{\partial R}\right)^2 P^2{}_{R} \qquad (7)$$

The above expression is simplified is simplified by substituting the partial derivatives,

$$\left(\frac{P_\mu}{\mu}\right)^2 = \left(\frac{P_{F_C}}{F_C}\right)^2 + \left(\frac{P_{F_N}}{F_N}\right)^2 + \left(\frac{P_{L_C}}{L_C}\right)^2 + \left(\frac{P_R}{R}\right)^2 \qquad (8)$$

The loads used for F_c and F_N were calibrated against the same standard. Those loads were measured by using a Shimadzu BX3200H. The scale has a resolution of 0.01gm. Therefore, the precision limit for load measurement is estimated to be ±0.005gm. The device has a linearity of 0.02gm. This linearity is used as bias.

Table: 3.8 Bias and precision limits of friction variables and nominal values

Variable	Bias limit	Precision limit	Nominal value
F_C	0.02gm	0.005gm	677.5gm
F_N	0.02gm	0.005gm	5397.6gm
L_C	±0.03mm	±0.005mm	50mm
R	±0.03mm	±0.005mm	10.5mm

Table 3.8 summarizes the nominal values, bias, and precision limits. Substituting these values in equations 5 and 8, the bias and precision limits typical for gray cast iron sliding against brake material at 1m/s and 1MPa are obtained as follows:

$$\left(\frac{B_\mu}{\mu}\right)^2 = 5.09\times10^{-6} \tag{9}$$

$$\left(\frac{P_\mu}{\mu}\right)^2 = 2.37\times10^{-7} \tag{10}$$

$$\left(\frac{U_\mu}{\mu}\right)^2 = \left(\frac{B_\mu}{\mu}\right)^2 + \left(\frac{P_\mu}{\mu}\right)^2 = 5.327\times10^{-6} \tag{11}$$

$$\left(\frac{U_\mu}{\mu}\right) = 2.308\times10^{-3} = 0.23\% \tag{12}$$

Therefore, the uncertainty in measuring friction coefficient (with 95% coverage) is 0.23%.

The precision limit due to sample-to-sample variation in tribocouple composition is found to be,

$\left(P_\mu\right)_{mat} = 0.2087$

The average friction coefficient $\bar{\mu} = 0.532$

Uncertainty in the average friction coefficient $U_{\bar{\mu}} = 0.12$

Therefore, the average friction coefficient value with 95% coverage is 0.54 ± 0.12.

CHAPTER 4

RESULTS AND DISCUSSION

4.1 Microstructure

4.1.1 AA6061/Al_2O_3/20p composite

The most important aspect of the microstructure in a particle-reinforced metal matrix composite is the distribution of the reinforcing particles, and this depends on the processing and fabrication routes involved. However, particles can modify other aspects of the matrix microstructure. In powder-processed material, the reinforcement distribution will depend on the blending and consolidation procedures, as well as the relative size of the matrix and reinforcing particles.

Figure 4.1 shows the microstructure of AA6061/Al_2O_3/20p composite, where the reinforced particles were generally equiaxed in shape. The Al_2O_3 reinforcement particles were of near-uniform shape. However, very few of the reinforcing particles were irregularly shaped, and these were dispersed randomly through the matrix. Particle clustering indicated by A and particle-depleted regions indicated by B were observed occasionally. EDX analysis revealed the composition of AA6061/Al_2O_3/20p as follows: C-1.46%, O-29.56%, Mg-0.83%, Al-68.48%, Si-0.45%.

4.1.2 Gray cast iron

Figure 4.2 shows the microstructure of gray cast iron. The microstructure consists of fine lamellar pearlite (indicated by A) with randomly distributed graphite flakes (indicated by B). The flake graphite pattern is identified to be of type A according to the ASTM A 247 specifications. The Type A arrangement indicates uniform distribution of graphite flakes with random orientation. The combination of this microstructure and the graphite flake arrangement is believed to exhibit better wear and friction in cast iron [45]. EDX analysis revealed the composition of gray cast iron as follows: C-8.13%, Si-2.16%, Ca-0.325%, Cu-0.81%, Fe-89.23%.

4.1.3 Brake pad material

A commercial semi-metallic brake pad material was used as a counterbody material. The sample was examined by using a scanning electron microscope (SEM). Figure 4.3 shows the distribution of the different ingredients. The SEM/EDS analysis showed the existence of the following elements in the brake pad material: C, N, Cu, Al, Ti, S, K, Fe, Mn, Ca, Zn, Si and O. Fig.4.4 shows the composition spectrum of the brake pad material. Because a single material cannot successfully meet the friction materials' general-purpose requirements, automotive friction material usually consists of several ingredients bound into a composite. Semi-metallic linings are a mixture of fragments or powdered metal held together with phenolic resins and other binders and fillers. The metal is present to improve heat transfer, and the amount present depends upon the specific heat transfer requirements. Therefore, the brake material includes iron and steel (e.g., steel wool and iron sponge) and titanium (high heat transfer coefficients). Existence

of sulphur indicates the presence of metal sulphides that acts as a solid lubricant. The purpose of the addition of copper and manganese is to reduce the metal pickup of the rotor by the friction material during braking.

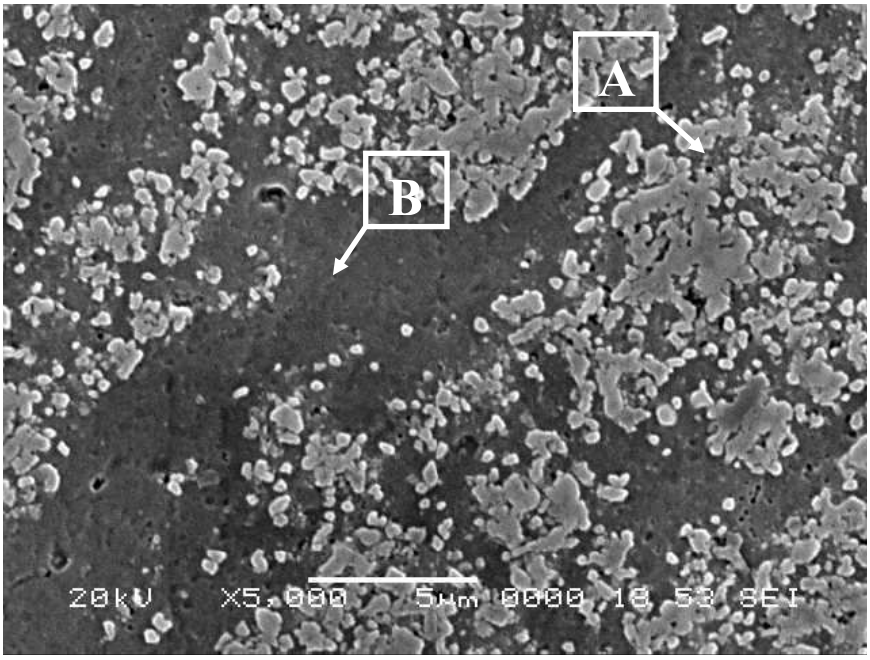

Figure 4.1 SEM micrograph showing etched microstructure of AA6061/Al_2O_3/20p

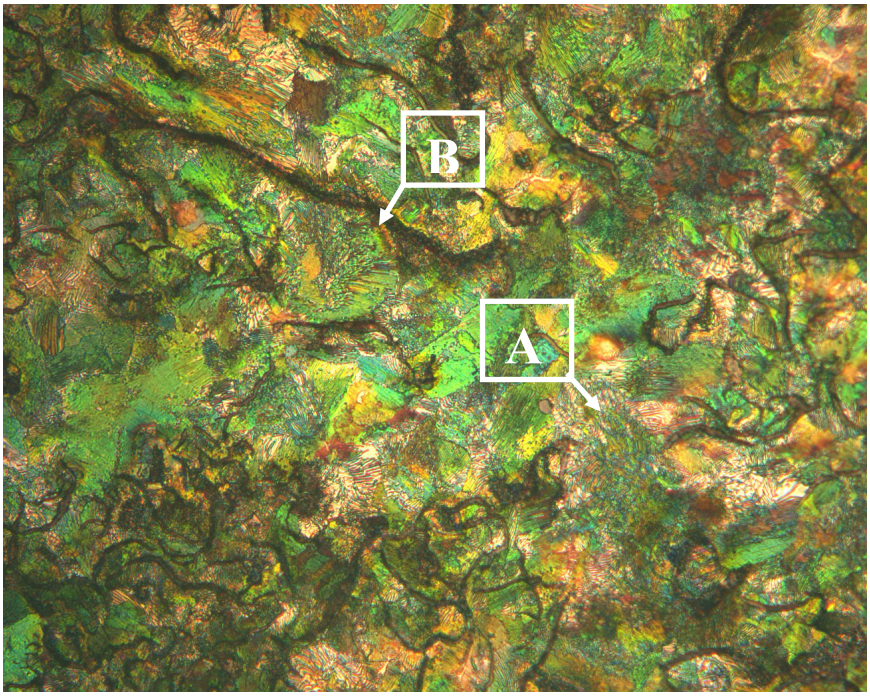

Figure 4.2 Optical micrograph of gray cast iron at X100 magnification

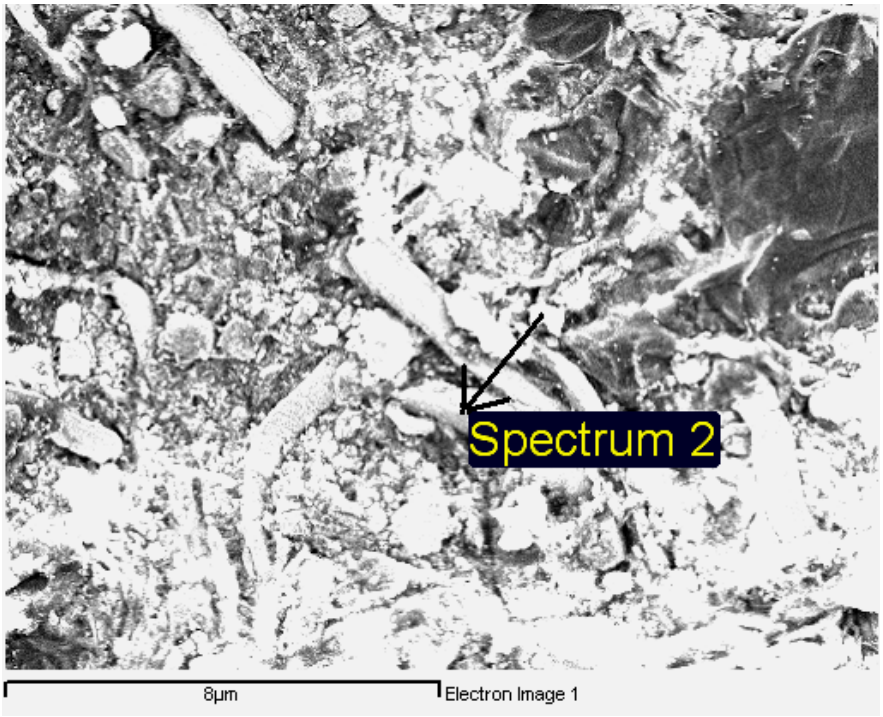

Figure 4.3 SEM micrograph of brake pad material

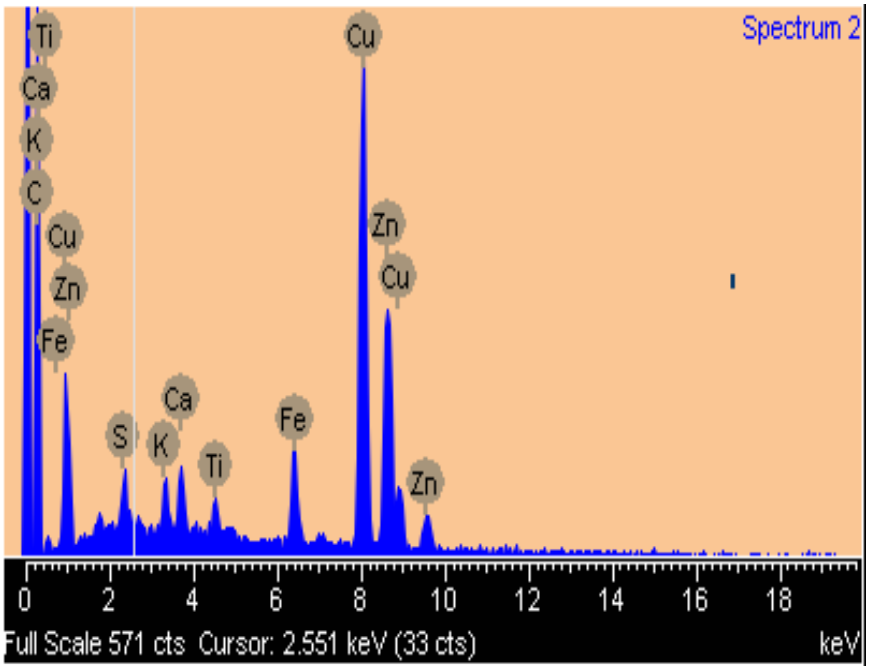

Figure 4.4 Composition spectrum of brake pad material

4.2 Microhardness

The results of hardness tests performed on Al6061-20% Al_2O_3 reinforced composite (AA6061/Al_2O_3/20p) and gray cast iron are shown in table 4.1. The average Vicker's hardness for AA6061/Al_2O_3/20p is (135.6±7.6) HVN. For gray cast iron, the average Vicker's hardness is (254.5±21) HVN. The average Vicker's hardness for semi-metallic brake pad material is (137±2.5) HVN. Hardness measurements were done thrice on each sample, and the average value is reported in table 4.1. Gray cast iron is harder than AA6061/Al_2O_3/20p composite and the semi metallic brake pad material.

Table 4.1 Hardness test results

S. No.	Material	Sample No.	Average Vicker's Hardness Number, HVN
1	AA6061/Al_2O_3/20p	1	130.1
2	AA6061/Al_2O_3/20p	2	132.4
3	AA6061/Al_2O_3/20p	3	144.3
4	Gray cast iron	1	235.8
5	Gray cast iron	2	250.8
6	Gray cast iron	3	277.0
7	Semi-metallic brake pad material	1	137
8	Semi-metallic brake pad material	2	140
9	Semi-metallic brake pad material	3	135

4.3 Gray cast iron-brake material tribo-couple wear

Gray cast iron was run against a semi-metallic brake pad material at the varying sliding velocities (1m/s, 1.5m/s, 2m/s, and 2.5m/s) and normal stresses (1MPa, 2MPa, and 3MPa). At each data point, the experiment was repeated thrice, and the average value with the standard error of mean was used as error bar. The wear rate uncertainties due to sample-to-sample variation of gray cast iron and the brake pad material were found to be 2-23 and 4-10 times greater than the instrument uncertainty. The contact temperatures were recorded by using a thermocouple placed close to the interface from the gray cast iron side. The variation of the wear rate of gray cast iron with the normal stress and the sliding velocity is discussed in 4.3.1. The variation of the wear rate of semi-metallic brake pad material with the normal stress and the sliding velocity is discussed in 4.3.2. The variation of the coefficient of friction with the normal stress and the sliding velocities is discussed in 4.3.3. The uncertainties in friction coefficient due to sample-to-sample variation were found to be 1.1-1.7 times greater than the instrument uncertainty. The precision error due to reading from the friction coefficient histogram was found to be negligible. The worn surfaces of gray cast iron show dark gray color patches covering the entire wear track when viewed with the naked eye. It is termed as tribo-layer, friction layer or film. The friction film is a layer of compacted wear particles originated from the friction material and the gray cast iron. The thickness of the friction film is measured by using a Fowler IP54 electronic outside micrometer with an accuracy of 0.0013mm. The thickness varied from 21.6 to 52 μm. A part of the friction film was scraped off the contact surface on the gray cast iron sample. The height of the sample with and without

friction film was measured. The difference in height gave the film thickness. These layers were characterized for their composition and topography.

4.3.1 Gray cast iron wear rate

In the first phase, the wear of the gray cast iron and the brake pad material found from several tests conducted at different loads and speeds. The variation of wear with load and sliding velocity, with cast iron sliding against brake pad material, is shown in Figure 4.5. The trend is not consistent for 2MPa and 3MPa normal stresses. For these stresses, the wear rate first increases (from $0.32mm^3/km$ and $0.71mm^3/km$ to $0.51mm^3/km$ to $0.78mm^3/km$ respectively) with an increase in the sliding velocity from 1m/s to 1.5m/s. Then it decreases (to $0.141mm^3/km$ and $0.265mm^3/km$ respectively) with an increase in the sliding velocity to 2m/s. It is again followed by an increase (to 0.466 mm^3/km and $0.654mm^3/km$ respectively) with a further increase in the sliding velocity to 2.5m/s. However, a consistent decrease in the wear rate (from $1.5mm^3/km$ to $0.16mm^3/km$) with an increase in the sliding velocity from 1m/s to 2m/s is observed for the 1MPa load. This is followed by a slight increase in the wear rate (to $0.26mm^3/km$) with an increase in the sliding velocity to 2.5m/s.

Results presented by Howell and Ball [30] also show a decrease in the wear rate of gray cast iron sliding against semi-metallic brake pad material at the applied normal stress of 1MPa. It was observed that the specific wear rate first decreased with the increasing sliding velocity. It was then followed by an increase with a further increase in the sliding velocity. However, the data points at which these changes occurred differ

from the present results. This may be due to the different composition of brake pad material used. In the work presented by Natarajan [9], the range of power used (0.625 MPa-m/s to 8.2 MPa-m/s) was similar to that (1MPa-m/s to 7.5MPa-m/s) used in the present study. But there was an increase in the wear rate with the increasing sliding velocity. Different composition of the brake pad material may be the possible reason. Asbestos fibers were used in the semi-metallic brake pad material in Natarajan's [9] work.

For a given sliding velocity, the wear is low at lower applied loads, and it increases with the load. As the applied load is increased, the wear is found to increase, except the increase in normal stress from 1MPa to 2MPa at 2m/s. Higher wear is observed for the maximum load. In the present research, the tendency of increasing the wear with increasing normal load is in agreement with Natarajan's results [9]. It is also in agreement with Howell and Ball's results [30]. However, a discrepancy in trend is observed at 1MPa load and 1m/s. The wear rate overshoots (the cause for this discrepancy is discussed in the following paragraphs).

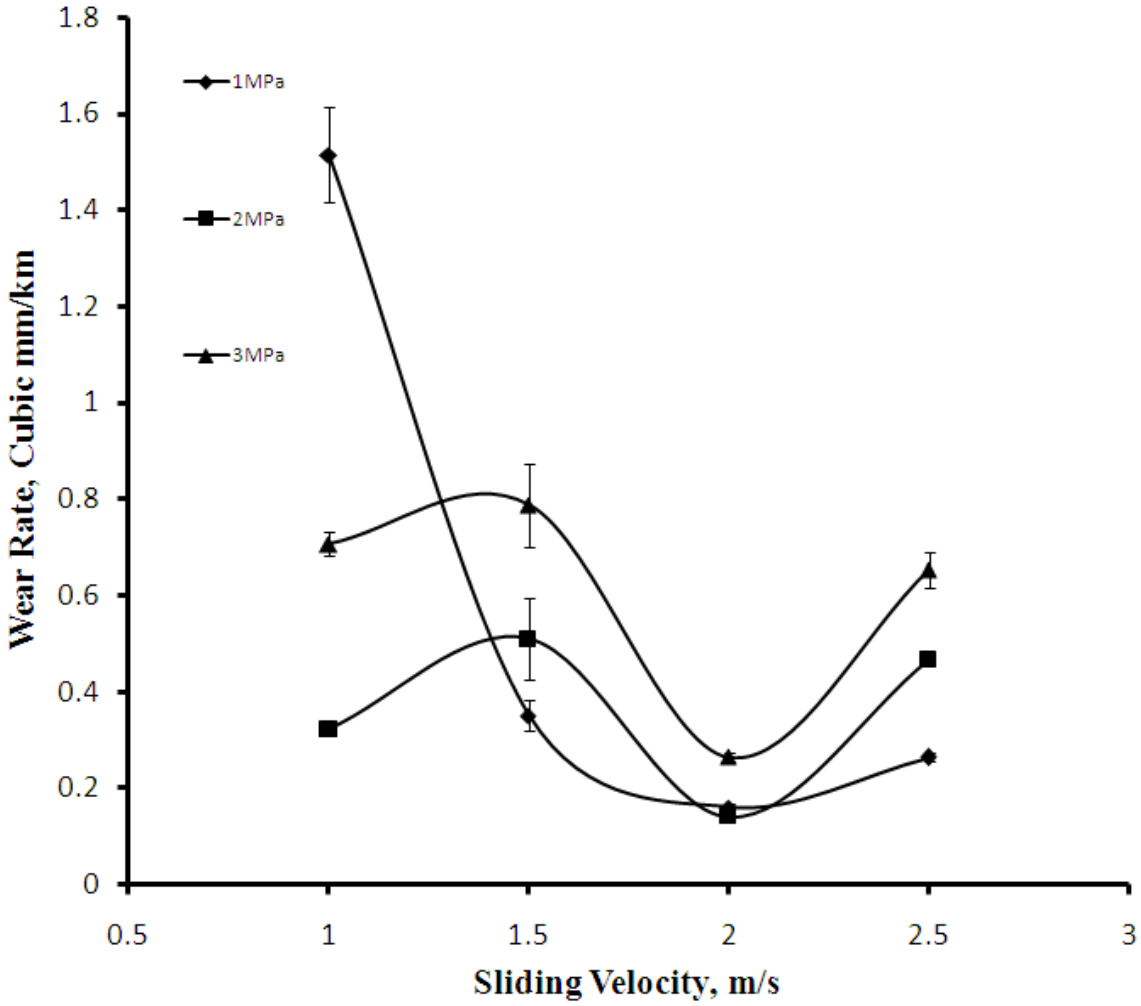

Figure 4.5 Wear rate of gray cast iron

SEM micrographs in Figures 4.6 - 4.8 show the deformation signs at the worn surfaces of gray cast iron drysliding against semi-metallic brake pad material. SEM micrographs were captured on samples run at different sliding velocities maintaining a constant load. Figure 4.6 (a) depicts a shallow crater (A) from where material has been removed in a surface with fine abrasion grooves at the sliding velocity of 1m/s and the normal stress of 1MPa. With the increasing sliding velocity, the roughness of the surface decreases as seen from Figures 4.6 (a)-(c). The transfer film appears to cover the surface

progressively with the sliding velocity increasing from 1m/s to 2m/s. Worn surfaces in Figure 4.6 (c) and (d) show that the further increase in sliding velocity to 2.5m/s results in the removal of material from the friction film (B). Figures 4.7 (a) and (b) show the wear scars representative of mild (A) and severe (B) wears at the normal stress of 2MPa and the sliding velocities of 1m/s and 1.5m/s. It is clear that mild wear behavior is characterized by smooth wear scars with fine features [20] (Figure 4.7a). Large and rough wear scars with coarse features characterize severe wear [20] (Figure 4.7b).

Figure 4.7 (d) shows that a large flake (D) of the friction film is removed at the sliding velocity of 2.5m/s in comparison to the small contact plateaus (C) shown in Figure 4.7 (c) at the sliding velocity of 2m/s. Friction film is seen to cover the surface with very small patches. These small patches indicate that a little material has been removed from the transfer layer.

Figure 4.8 (a) shows that the friction film is peeled off in the form of larger platelets (A) at the normal stress of 3MPa and a sliding velocity of 1m/s. The intense wear of the transfer layer in the form of flakes and fine wear particles (B) was observed with the increase in the sliding velocity to 1.5m/s as shown in Figure 4.8 (b). Figure 4.8 (c) again shows that most of the surface is covered with the transfer layer with rough granular patches (C) with the increase in the sliding velocity to 2m/s. With the increase in the sliding velocity to 2.5m/s, the transfer film is again peeled off in the form of larger platelets (D) and the base material is exposed as shown in Figure 4.8 (d).

From microstructural examination, it can be inferred that there is less formation of transfer film at the interface at low applied load (1MPa) and sliding velocity (1m/s). EDX

analysis of the worn surface of gray cast iron revealed the existence of the following elements by weight percentages: Fe-89.57%, Si-2.06%. This is almost close to the composition of base material (refer 4.1.2). Therefore, it can be concluded that there is less formation of friction film. Harder asperities in brake pad material abraded the gray cast iron, resulting in a higher wear rate. With the increase in the sliding speed, there will be less time for material to escape from the wear track. Indirectly, this will imply that, at higher sliding velocities, the formation of transfer film is fast. The load-carrying friction film formation at the interface leads to an increased real contact area, resulting in a decrease in the applied pressure. The wear rate decreased with an increase in the applied load to 2MPa. This can be explained by saying that the increased load reduced the space between the gray cast iron and the brake pad material. When the height between them is reduced, more debris will become jammed. As a result, wear debris will be more prone to sinter, forming agglomerates or even continuous films. A continuous film or agglomerates on the specimen caused lubrication [46 - 48]. Therefore, the wear rate decreased with an increase in the load. At higher velocities and at higher loads, the formation and destruction of transfer film is fast. In addition, the temperature rise is high. As a result, a fluctuation in the wear rate with the increasing sliding speed is observed at higher loads of 2MPa and 3MPa. That is, a lower wear rate is observed at a sliding velocity of 2m/s and normal stresses of 2MPa and 3MPa, due to the formation of friction film. Therefore, the formation of transfer film appears to act as a protective layer for gray cast iron.

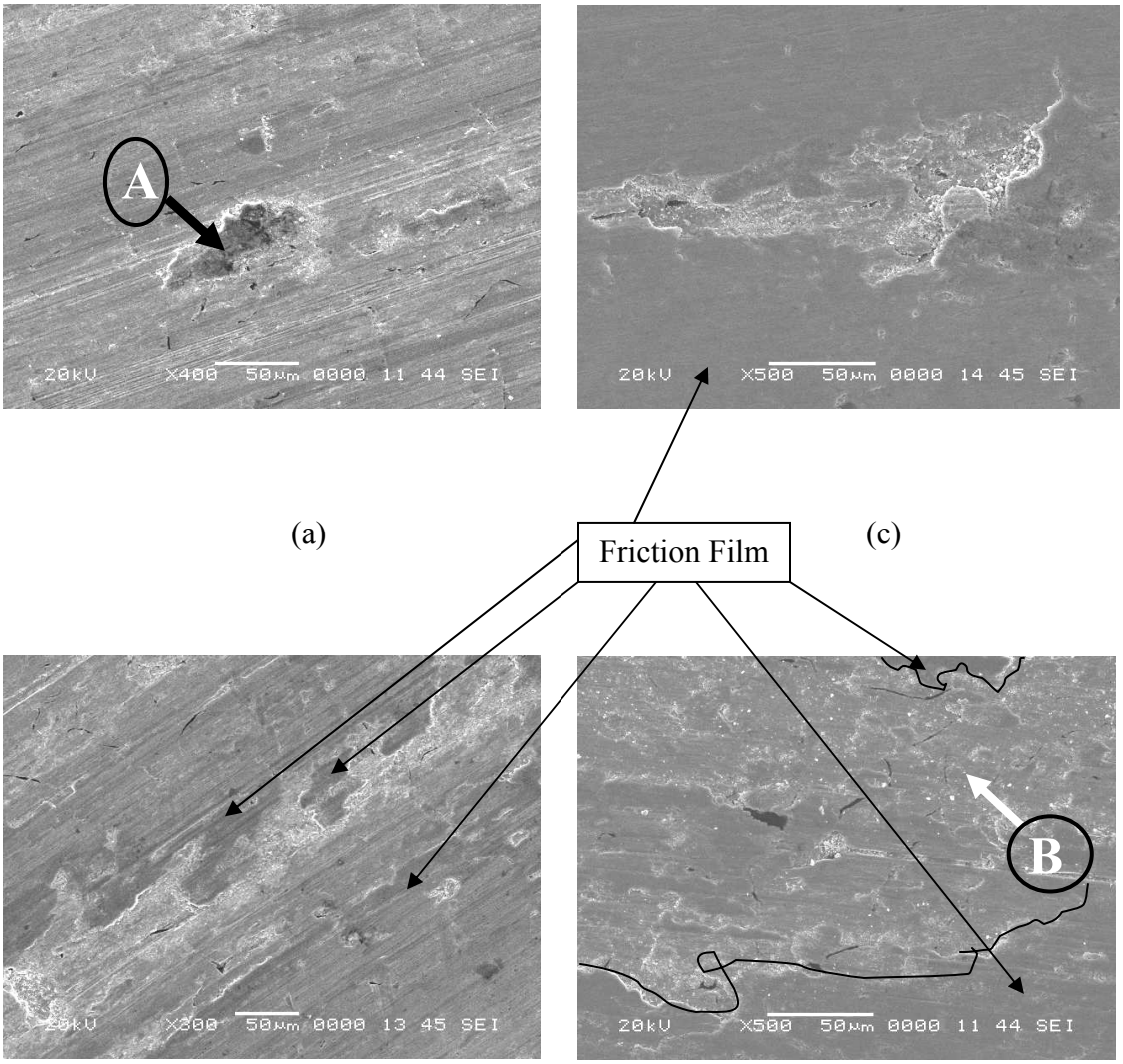

Figure 4.6.SEM micrographs of gray cast iron worn surface under 1MPa normal stress and sliding velocities of (a) 1m/s, (b) 1.5m/s, (c) 2m/s, (d) 2.5m/s.

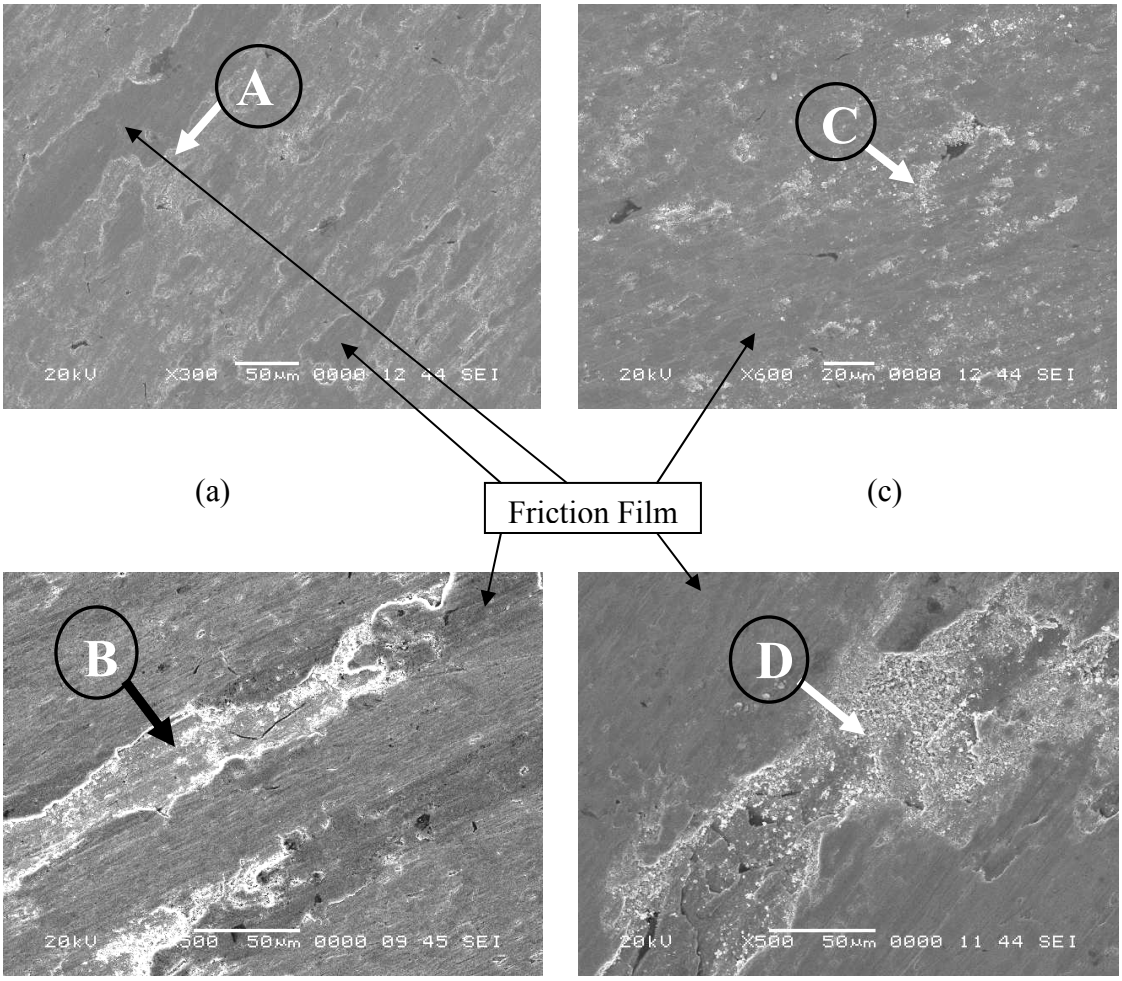

Figure 4.7.SEM micrographs of gray cast iron worn surface under 2MPa normal stress and sliding velocities of (a) 1m/s, (b) 1.5m/s, (c) 2m/s, (d) 2.5m/s.

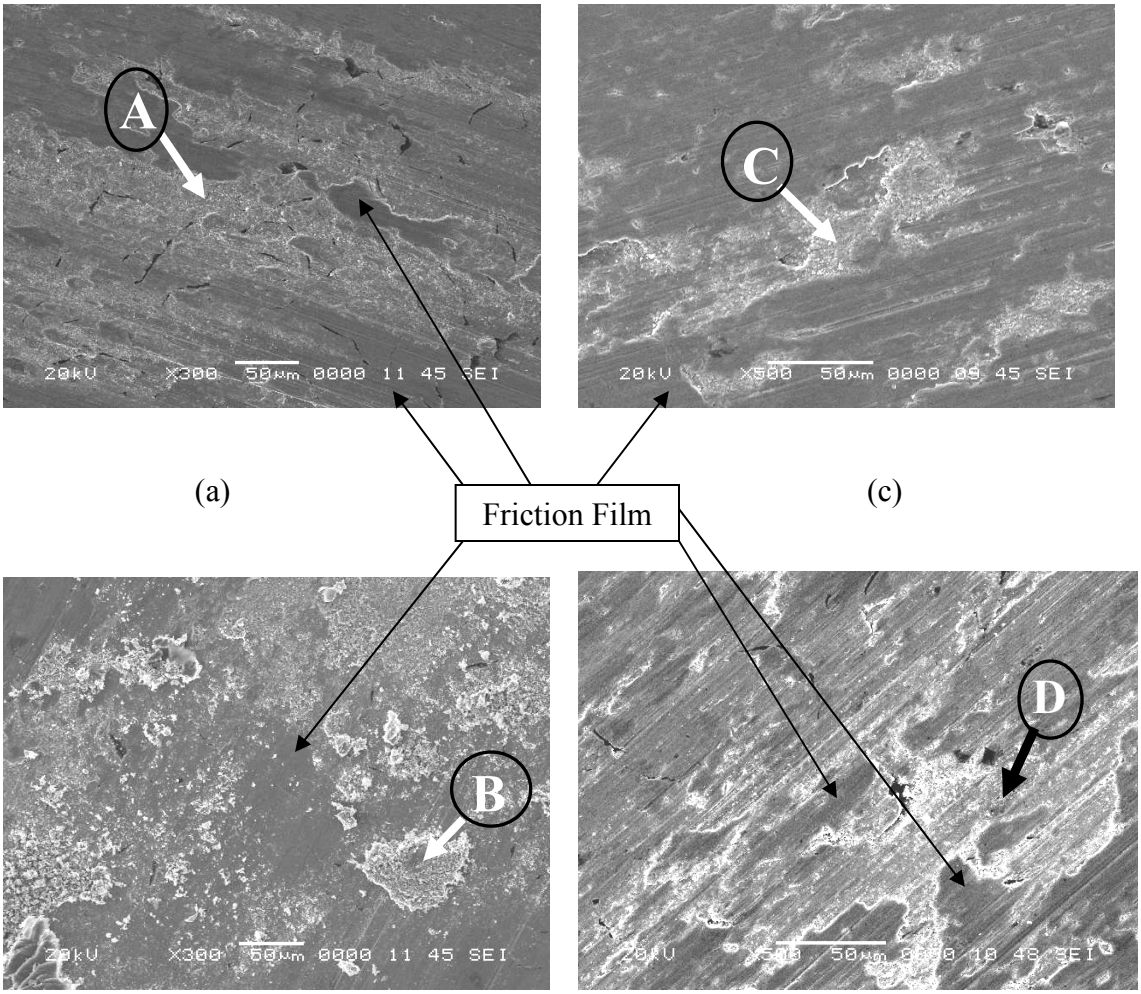

Figure 4.8.SEM micrographs of gray cast iron worn surface under 3MPa normal stress and sliding velocities of (a) 1m/s, (b) 1.5m/s, (c) 2m/s, (d) 2.5m

4.3.2 Wear rate brake pad material sliding against gray cast iron

The variation of wear with load and sliding velocity for brake pad material sliding against gray cast iron is shown in Figure 4.9. The general trend shows the increase in the wear rate with the increase in the sliding velocity. It is in agreement with the work presented by Natarajan [9]. However, a higher wear rate (3.8mm^3/km) is observed at the normal stress of 1MPa and the sliding velocity of 1m/s respectively. The wear rate then decreases (1.47mm^3/km) with the increase in the sliding velocity to 1.5m/s. No significant change is observed with the further increase in the sliding velocity to 2.5m/s. Results presented by Howell and Ball [30] show similar behavior for the semi-metallic brake pad material sliding against gray cast iron at the applied normal stress of 1MPa. The trend is not consistent for 2MPa normal stress. The wear rate first increases (from 2.33mm^3/km to 3.72mm^3/km) with an increase in the sliding velocity from 1m/s to 1.5m/s. Then it decreases slightly (to 3.1mm^3/km) with an increase in the sliding velocity to 2m/s. It is again followed by a slight increase (to 3.5mm^3/km) with a further increase in the sliding velocity to 2.5m/s. At 3MPa load, the wear rate first increases with an increase in the sliding velocity from 1m/s to 1.5m/s. No significant change in the wear rate is observed with increase in sliding velocity to 2m/s. An abrupt increase in wear rate (from 4.46mm^3/km to 15.67mm^3/km) is observed with an increase in the sliding velocity from 2m/s to 2.5m/s.

At a given sliding velocity, the wear is low at lower values of normal stresses, but it increases with stress. At lower loads, the contact plateaus and temperature rise are low. So at lower loads, reduced wear is observed. As the applied normal stress is increased, the wear loss is found to increase. Higher wear is observed for the maximum normal stress. In the present study, the tendency of the increasing wear with the increasing normal load is in agreement with Natarajan's [9] results. As the normal stress is increased from 1MPa to 2MPa at 1m/s sliding velocity, the wear rate is observed to decrease. The wear rate then increases with an increase in the load to 3MPa. However, the wear rate is found to overshoot at 3MPa load and 2.5m/s sliding velocity.

The maximum wear rate is observed at the normal stress of 3MPa and a sliding velocity of 2.5m/s. The maximum wear rate ($2.4x10^{-7}mm^3/KJ$) obtained in the present research is very low compared to the maximum wear ($6.1mm^3/KJ$) provided by the manufacturer. This is because of the difference in the operating conditions (sliding velocity of 50.8m/s and pressure-14MPa).

From microstructural examination (Figures 4.6 - 4.8) it can be inferred that there is less formation of transfer film at the interface at low applied load and sliding velocity. This can be the reason for the high wear rate of gray cast iron running at 1m/s at 1MPa. EDX analysis of the worn surface of gray cast iron revealed the existence of the following elements by weight percentages: Fe-89.57%, Si-2.06%. This is close to the composition of base material (refer 4.1.2). Therefore, it can be concluded that there is less formation of friction film. Hence, gray cast iron with a higher hardness (254.5 HVN) caused much wear of the relatively softer brake pad material (137 HVN). This can be the reason for the high wear rate of the brake pad material running at 1m/s at 1MPa. At

higher loads, the gray cast iron is forced against the brake pad material, resulting in high temperature at the interface, and thereby destroying the transfer film at a faster rate. So new transfer films are formed faster, enhancing the wear of the lining. With an increase in the sliding speed, there will be less time for material to escape from the wear track. Indirectly, this will imply that, at higher sliding velocities, the formation of transfer film is fast. The load-carrying friction film formation at the interface leads to an increased real contact area, resulting in a decrease in the applied pressure. This results in effective reduction in wear. The eventual destruction in the transfer film leads to a decreased real contact area, resulting in an increase in the applied pressure. At higher velocities and at higher loads, the formation and destruction of the transfer film is fast. As a result, a fluctuation in the wear rate with the increasing sliding speed is observed at normal stress of 2MPa. Therefore, formation of friction film appears to act as a protective layer for brake pad material also. The average interface temperature recorded at 3MPa normal stress and 2.5m/s is 251°C. The abrupt increase in the wear rate is due to degradation of friction material. The literature shows that the onset of degradation of semi-metallic friction material starts at 230°C. The wear of friction materials remains insensitive to temperature up to about 230°C (drum), but it increases exponentially at higher temperatures [49]. Above the degradation temperature, the binding properties of resin become weak. When this happens, the wear rate increases exponentially as observed by Liu [49].

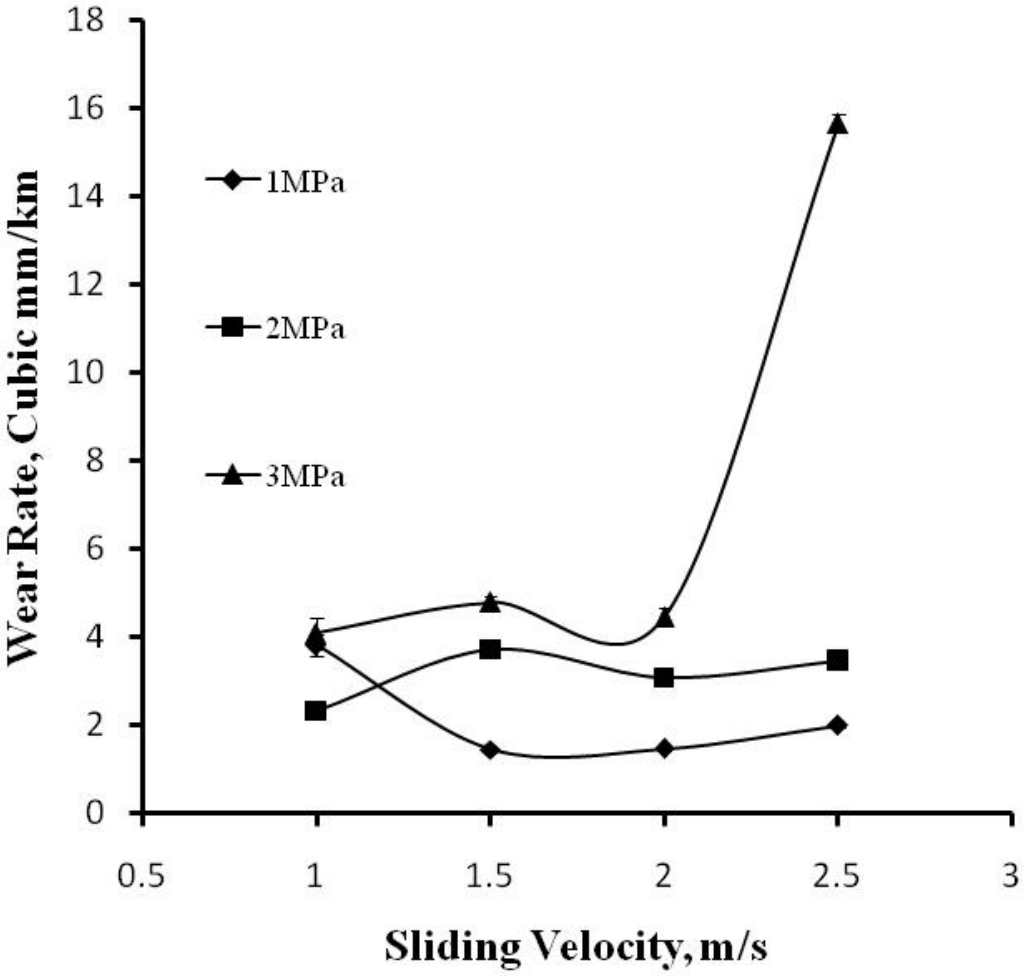

Figure 4.9 Wear rate of brake pad material

4.3.3 Coefficient of friction

Variation of the friction coefficient with the sliding velocity and normal stress is shown in Figure 4.10. The general trend shows the decrease in the friction coefficient with the sliding velocity. This is in agreement with the results presented by Howell and Ball [30], which shows a uniform decrease in the coefficient of friction with gray cast iron sliding against semi-metallic brake pad material at the applied normal stress of 1MPa. But the results presented by Natarajan [9] show a uniform increase in the coefficient of friction with gray cast iron sliding against semi-metallic brake pad material with increasing sliding velocity. This might be due to the different composition of the brake pad material used. A very low weight percentage (4%) of copper and the asbestos fiber was used in the semi-metallic brake pad material. It is found to increase with normal stress at lower sliding velocities (1m/s and 1.5m/s) and to decrease at higher sliding velocities (2m/s and 2.5m/s).

At a low applied stress of 1MPa and a sliding velocity of 1m/s, the friction coefficient is high (0.532) due to less formation of friction film at the interface. At higher sliding velocities, the formation of friction film is fast. Hence, the friction coefficient is found to decrease (to 0.466) with the increase in the sliding velocity to 1.5m/s. It is followed by an increase in the friction coefficient at a slow rate. This increase can be due to the increasing content of copper in the friction film, as evident from EDX analysis (Table 4.2). The copper powder is frequently used in heavy-duty linings to break up transfer films and to improve the fade performance [50]. Mutlu [51] observed that the friction coefficient increased (from 0.26 to 0.39) with the increment of copper

percentages (from 15% to 25%). The slow rate of increase in the friction coefficient at lower normal stress indicates that the friction film is stable for more time and the temperature rise is low.

At a normal stress of 2MPa, the friction coefficient decreased (from 0.436 to 0.3689) with the sliding velocity except at 1.5m/s. EDX analysis of friction film (obtained at 2MPa and 1.5m/s) reveals the existence of a high content of carbon and nitrogen (Table 4.2). This indicates the presence of phenolic resin. The resin causes the high steady-state friction coefficient (0.454) and poor wear resistance [52, 53]. The friction coefficient is found to decrease (from 0.535 to 0.352) with the increasing sliding velocity up to 2m/s at 3MPa normal stress. An abrupt increase (to 0.417) is observed at the sliding velocity of 2.5m/s. The interface temperature recorded at this data point is 251°C. EDX analysis of friction film revealed the existence of carbon and nitrogen (Table 4.2). It can be concluded from this result that, at higher velocity and at higher loads, the formation and destruction of the transfer film is fast, which results in friction fade (reduction in friction) and subsequent recovery.

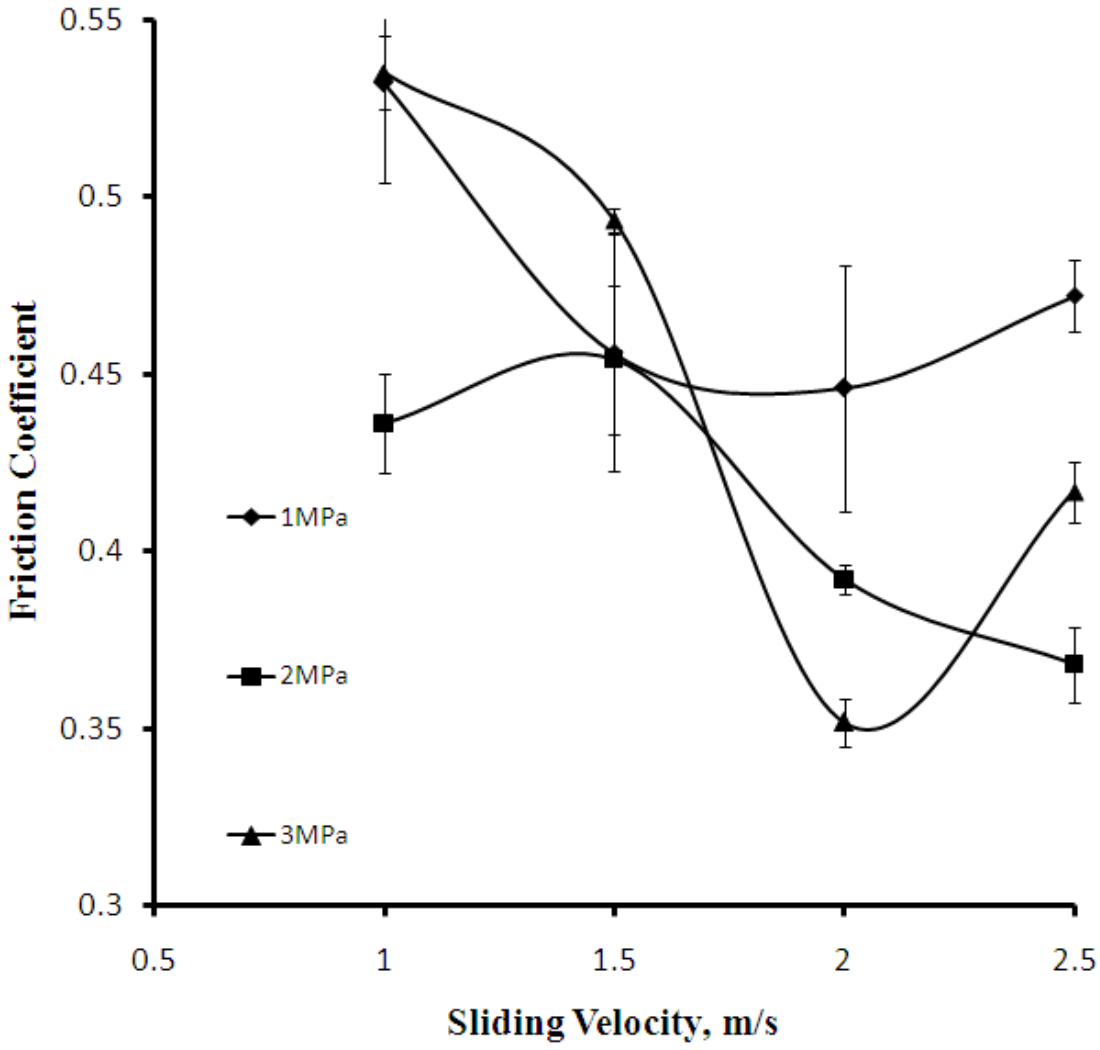

Figure 4.10 Friction coefficient for brake pad material sliding against gray cast iron

Table 4.2: EDX analysis results and interface temperatures for gray cast iron

	1MPa	2MPa	3MPa
1m/s	Fe-89.57%,Si-2.06%, O-7.26%, T=57°C.	Cu-1.71%, T=68°C.	Cu-3.48%, T=**102**°C.
1.5m/s	Cu-1.35%, T=57°C.	C-10.83%, N-18.06% T=76°C.	Cu-3.02%, Al-43.99%, O-11.21%, T=**123**°C.
2m/s	Cu-2.83%, T=57°C.	Cu-1.12%, T=84°C.	Cu-0%, T=**143**°C.
2.5m/s	Cu-4.22%, T=70°C.	Cu-3.28%, S-0.57%, T=97°C.	C-4.46%, N-9.50%, O-19.08%, Si-1.22%, T=**251**°C.

4.4 AA6061/Al_2O_3/20p-brake material tribo-couple wear

AA6061/Al_2O_3/20p was run against a semi-metallic brake pad material at the varying sliding velocities (1m/s, 1.5m/s, 2m/s, and 2.5m/s) and normal stresses (1MPa, 2MPa, and 3MPa). At each data point, experiment was repeated thrice, and the average value with the standard error of mean is reported. The wear rate uncertainties of the AA6061/Al_2O_3/20p and the brake pad material were formed to be 4.5-25 and 1.6-70 times greater than the instrument uncertainty. The contact temperatures were recorded by using a thermocouple placed close to the interface from the composite side. The variation of the wear rate of the AA6061/Al_2O_3/20p composite with the normal stress and the

sliding velocities is discussed in 4.4.1. The variation of the wear rate of the semi-metallic brake pad material with the normal stress and the sliding velocities is discussed in 4.4.2. The variation of the coefficient of friction with the normal stress and the sliding velocities is discussed in 4.4.3. The uncertainties in the friction coefficient due to sample-to-sample variation were found to be 1.7 times greater than the instrument uncertainty. The precision error due to reading from the friction coefficient histogram was found to be negligible. The worn surfaces of the gray cast iron show dark gray color patches covering the entire wear track when viewed with the naked eye. It is termed as tribo-layer, friction layer or film. The friction film is a layer of compacted wear particles originating from the friction material and the gray cast iron. The thickness of the friction film is measured by using a Fowler IP54 electronic outside micrometer with an accuracy of 0.0013 mm. The thickness varied from 10-57 μm. A part of the friction film was scraped off the contact surface on the gray cast iron sample. The height of the sample with and without friction film was measured. The difference in height gives the film thickness. These layers are characterized for their composition and topography.

4.4.1 AA6061/Al_2O_3/20p composite wear rate

The wear of the AA6061/Al_2O_3/20p composite sliding against the semi-metallic friction material is found for various loads and sliding velocities. The variation of the wear rate with the sliding velocity and normal stress for AA6061/Al_2O_3/20p composite sliding against semi-metallic brake pad material is shown in Figure 4.11. The general trend shows that the wear rate decreases (63-75%) with the increase in the sliding velocity from 1m/s to 2m/s. It then increases (117-125%) with the increase in sliding velocity from 2m/s to 2.5m/s. This increase is observed to be negligible for 1MPa load. A

higher wear rate is observed at 2MPa load and 1.5m/s sliding velocity. Results presented by Howell and Ball [30] also show a constant specific wear rate of AMC sliding against semi-metallic brake pad material at the applied normal stress of 1MPa. Constant wear rates were established right from 0.5m/s to 3m/s sliding velocity. However, in the present investigation, a steady wear rate is established at 1.5m/s sliding velocity. Different composition of brake pad material, and the submicron size of Al_2O_3 reinforcement used , could be the possible reasons. In the work presented by Natarajan [9], the range of power used (0.625 MPa-m/s to 8.2 MPa-m/s) used was similar to that used in the present study (1MPa-m/s to 7.5MPa-m/s). But there was an increase in the wear rate with the increasing sliding velocity. Larger particulate reinforcement size (SiC-43μm) could be the possible reason. Different composition of brake pad material could be another possible reason. Asbestos fibers were used in the semi-metallic brake pad material in Natarajan's [9] work. Uyyuru [30] found very inconsistent behavior of wear with the increasing sliding velocity. Larger particulate reinforcement size (SiC-13μm) and a different composition of brake pad material used in his investigation could be the possible reason.

It was observed that the wear rate first decreases from 1MPa load to 2MPa load, but later increases with an increase in the load. A higher wear rate is observed at 1MPa and 1m/s sliding velocity. However, lower wear rates are observed at 1MPa load and sliding velocities from 1.5-2.5m/s. Results presented by Uyyuru [33, 34] also show a similar behavior. But, in the work presented by Natarajan [9], there was an increase in the wear rate with the increasing normal stresses, for the reasons already mentioned.

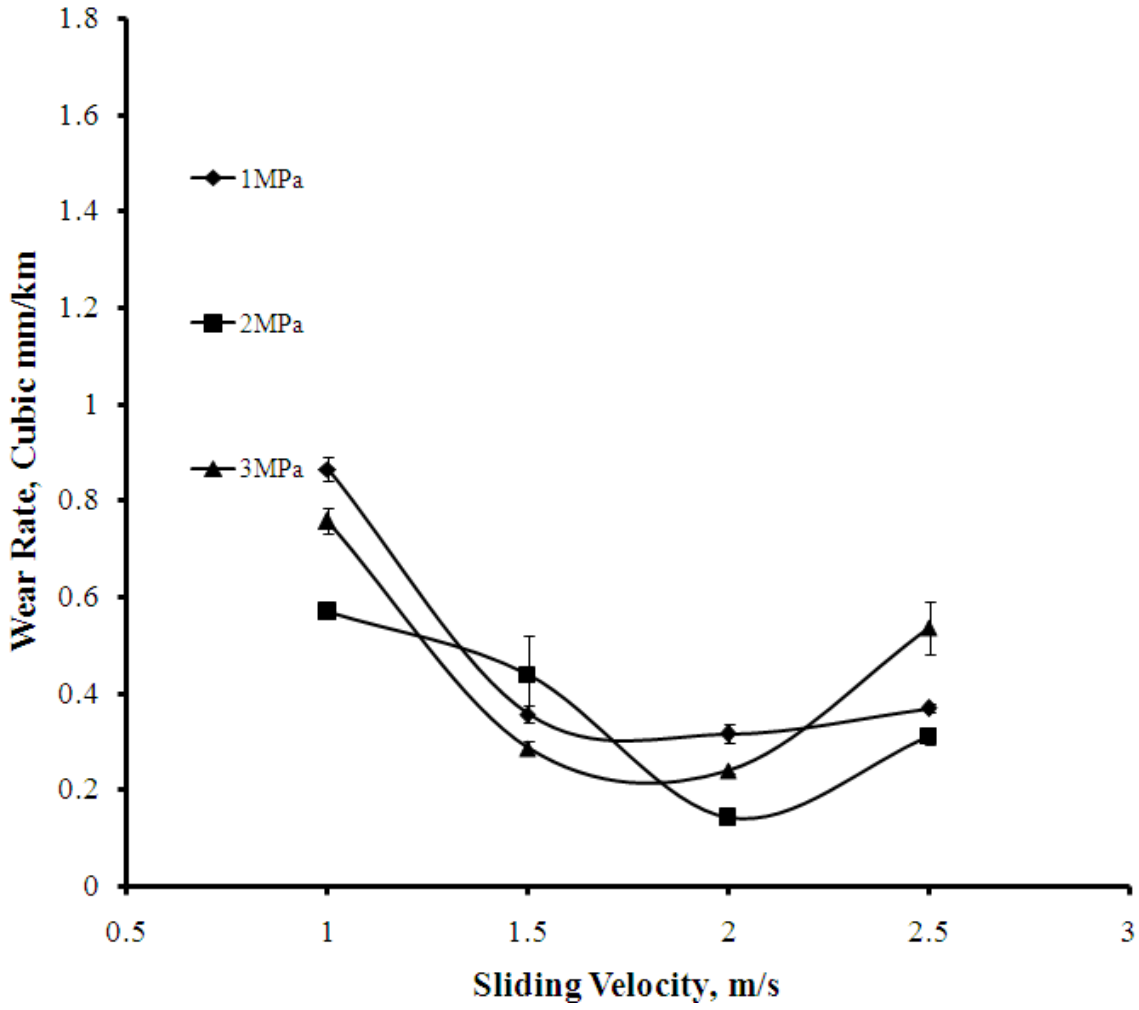

Figure 4.11 Wear rate of AA6061/Al_2O_3/20p sliding against brake pad material

The worn surfaces of AA6061/Al_2O_3/20p composite were microscopically examined by using SEM. Figures 4.12 – 4.14 show the deformation signs at the worn surfaces of AA6061/Al_2O_3/20p dry-sliding against semi-metallic brake pad material. SEM micrographs were captured on samples run at different sliding velocities while maintaining a constant load. Figure 4.12(a) show striations (A) on the AA6061/Al_2O_3/20p composite surface at the sliding velocity of 1m/s and the normal stress of 1MPa. With the increasing sliding velocity, the roughness of the surface

decreases as shown in Figures 4.12(a)-(d). The striations were observed to be formed on friction film. It is observed that the distance between striations increased with the increase in the sliding velocity. The increase in the sliding velocity from 1.5m/s to 2.5m/s does not cause much change in the surface morphology. This indicates that, at lower loads, friction film can be maintained for longer time. The worn surface in Figure 4.13(a) shows a large deep groove with flakes (A) at the normal stress of 1MPa and the sliding velocity of 1m/s. It is ploughing into the matrix material, and it indicates abrasive wear. The worn surface in Figure 4.13(b) shows that a layer of friction film is broken (B) with the increase in the sliding velocity to 1.5m/s. This shows that friction film forms in layers and after reaching certain thickness, it breaks. Figure 4.13(c) shows rough and coarse wear scars (C) indicative of mild wear with the increase in the sliding velocity to 2m/s. This shows that with the increase in the sliding velocity friction film forms again. Figure 4.13(d) shows fine wear scars (D) characteristic of severe wear with the increase in the sliding velocity to 2.5m/s. The large flake of the friction layer is observed to be removed. This shows that, at higher loads, formation and destruction of the friction layer are fast. Figure 4.14(a) shows a large crater (A) from where bulk material has been removed at the normal stress of 3MPa and the sliding velocity of 1m/s. It indicates adhesive wear. Striations were also observed on the worn surface. Figures 4.14(b) and 4.14(c) show that friction film covers most of the surface with characteristic features of mild wear. Figure 4.14(d) shows that friction film is destroyed and ceramic particles are exposed (B) with the increase in the sliding velocity to 2.5m/s.

From microstructural examination, it can be inferred that there is less formation of transfer film at the interface at the low applied load and sliding velocity. This can be the

reason for the high wear rate of AA6061/Al_2O_3/20p composite running at 1m/s at 1MPa. With the increase in the sliding speed, there will be less time for material to escape from the wear track. Indirectly, this will imply that, at higher sliding velocities, the formation of transfer film is fast. The load-carrying friction film formation at the interface leads to an increased real contact area, resulting in a decrease in the applied pressure. This results in an effective reduction in the wear. The eventual destruction in transfer film leads to a decreased real contact area, resulting in an increase in the applied pressure. At higher velocities and at higher loads, the formation and destruction of transfer film is found to be fast. In addition, the temperature rise is also high.

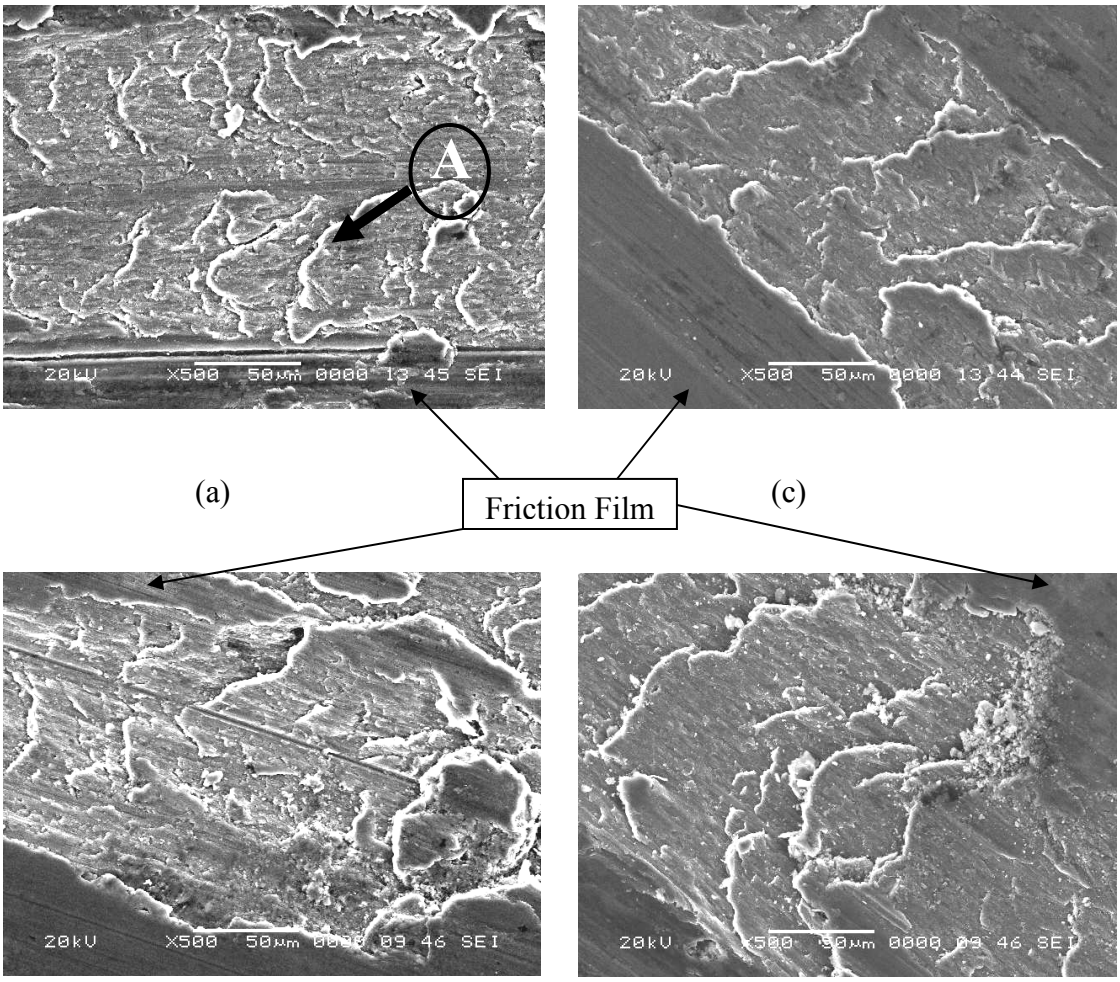

Figure 4.12.SEM micrographs of AA6061/Al_2O_3/20p composite worn surface under 1MPa normal stress and sliding velocities of (a) 1m/s, (b) 1.5m/s, (c) 2m/s, (d) 2.5m/s.

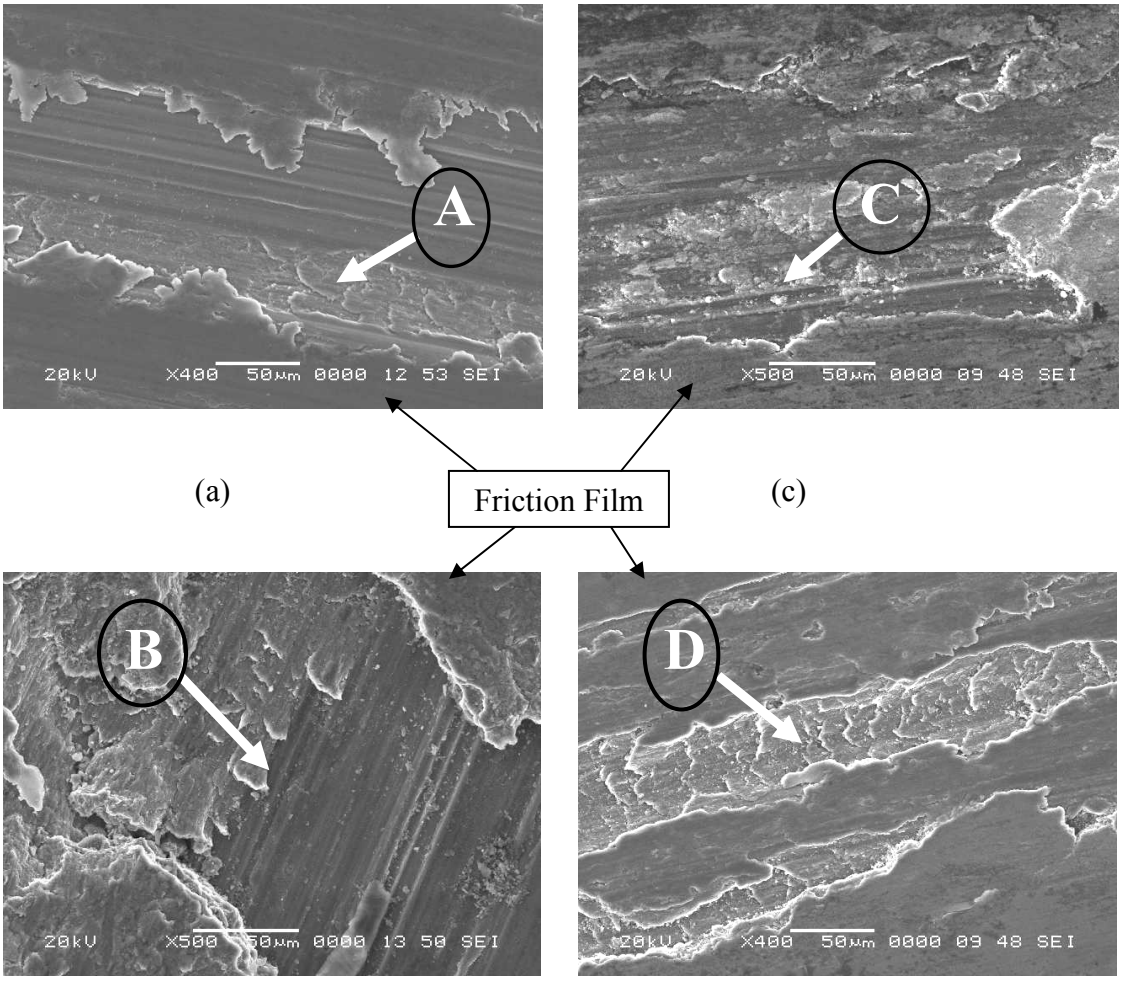

Figure 4.13.SEM micrographs of AA6061/Al_2O_3/20p composite worn surface under 2MPa normal stress and sliding velocities of (a) 1m/s, (b) 1.5m/s, (c) 2m/s, (d) 2.5m/s.

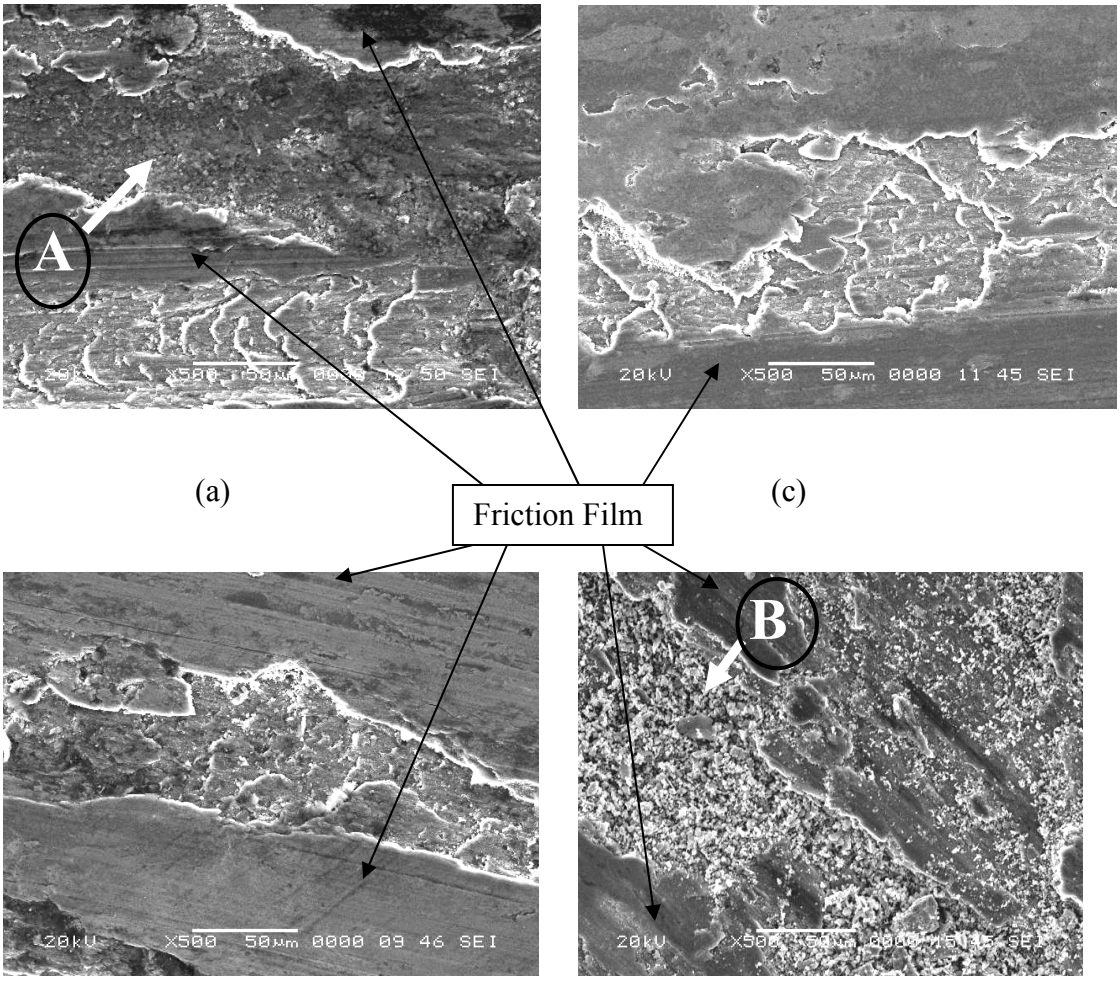

Figure 4.14.SEM micrographs of AA6061/Al_2O_3/20p composite worn surface under 3MPa normal stress and sliding velocities of (a) 1m/s, (b) 1.5m/s, (c) 2m/s, (d) 2.5m/s.

4.4.2 Wear rate of brake pad material sliding against AA6061/Al_2O_3/20p composite

The variation of wear rate with sliding velocity for AA6061/Al_2O_3/20p composite sliding against semi-metallic brake pad material is shown in Figure 4.15. The wear rate is found to increase (from 0.545mm^3/km and 3.6mm^3/km to 3.22mm^3/km and

8.74mm^3/km respectively) with the increase in the sliding velocity at normal stresses of 2MPa and 3MPa. The wear rate is found to increase with the increase in normal stress, and this increase is high for the higher loads. The highest wear rate (8.74 mm^3/km) is observed at the highest load and highest sliding velocity (3MPa and 2.5m/s respectively). No significant change is observed with the increase in the sliding velocity at the lowest applied stress of 1MPa. The results presented by Howell and Ball [30] show a disagreement with the present results. They found an increase in the wear rate of brake material with the increasing sliding velocity at 1MPa normal stress. Larger particulate reinforcement (Al_2O_3) size in the counterface used in their investigation may be the reason. In the work presented by Natarajan [9], there was also an increase in the wear rate with the increasing sliding velocity at 1.27MPa. The different composition of brake pad material may be the reason. Asbestos fibers were used in the semi-metallic brake pad material in Natarajan's [9] work. Larger particulate reinforcement size (SiC-43μm) in the counterface used in his investigation could be another reason.

From microstructural examination of Figures 4.12-4.14, it can be inferred that there is less formation of transfer film at the interface at 1MPa normal stress and 1m/s sliding velocity. No significant effect on the morphology of friction film is observed with the increase in the sliding velocity at 1MPa. It appears that friction film is maintained for various sliding velocities at low loads. As a result, no high fluctuations in the wear rate of brake material at 1MPa normal stress occur with the increasing sliding velocity. It can be suggested, at lower loads, that protruding Al_2O_3 particles are conducive to accommodate large amounts of transfer materials between two partners. The thick friction films formed this way protect the brake material from abrasion. Therefore, a nearly constant wear rate

is obtained at 1MPa. With an increase in the sliding speed, there will be less time for material to escape from the wear track. Indirectly, this will imply that, at higher sliding velocities, the formation of transfer film is fast. The load-carrying friction film formation at the interface leads to an increased real contact area, resulting in a decrease in the applied pressure. Therefore, a decrease in the wear rate was expected at 2MPa normal stress and 2m/s sliding velocity, due to the formation of friction film. But the Al_2O_3 particles, as seen in figure 4.12(c), were scoring the brake pad material. This resulted in an increase in the wear of the brake pad material. It can be suggested that the small-size Al_2O_3 are easily detached from Al matrix, due to the plastic deformation of AA6061/Al_2O_3/20p under the influence of higher load, sliding speed and contact temperature, and then they enter the thin friction films, which tends to abrade the brake material. The eventual destruction in the transfer film leads to a decreased real contact area, resulting in increase in the applied pressure. This leads to an effective increase in the wear rate. The highest wear rate was observed at maximum normal stress of 3MPa and sliding velocity of 2.5m/s. The protruding Al_2O_3 particles from the counterface destroy the transfer film, and they plough the brake pad material.

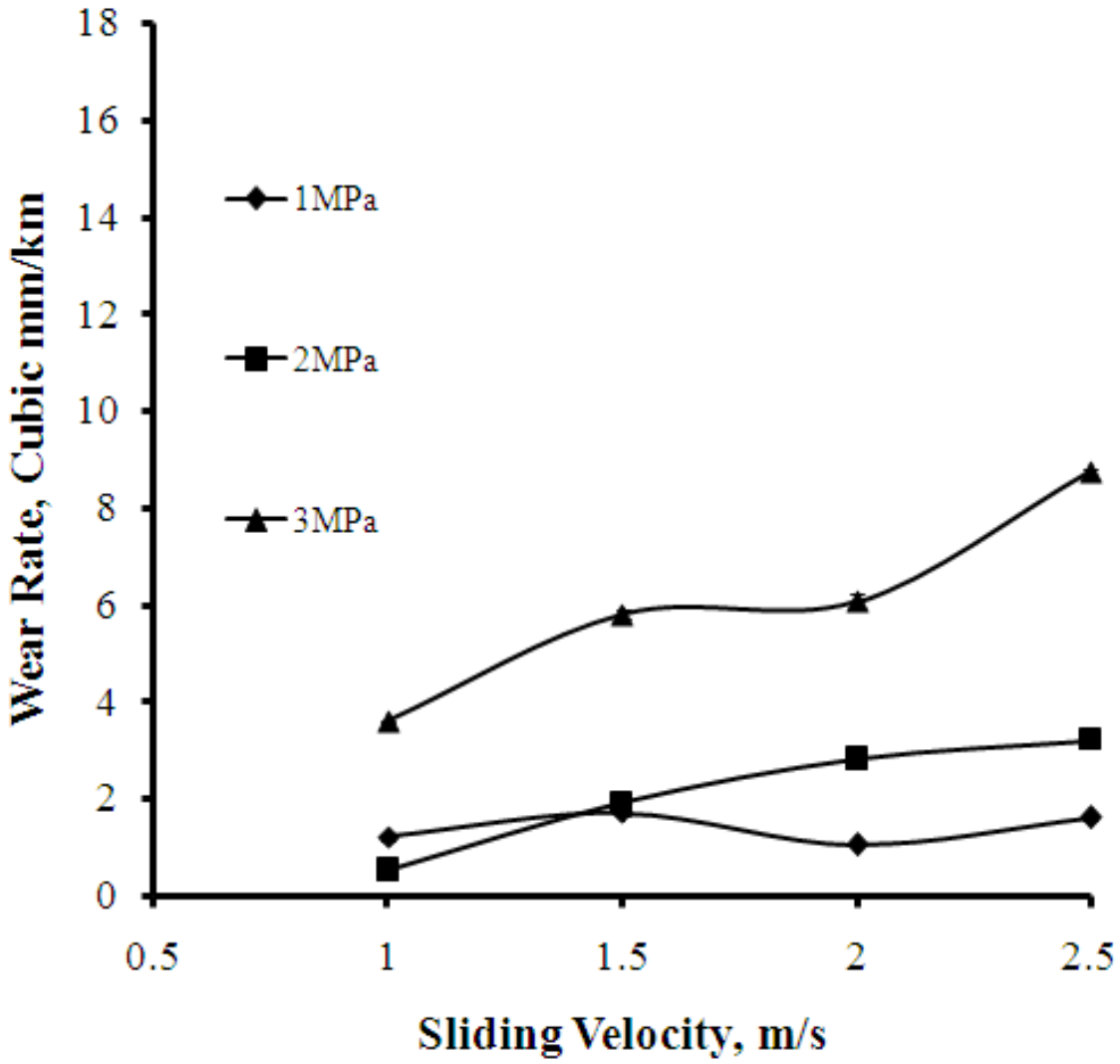

Figure 4.15 Wear rate of brake pad material sliding against AA6061/Al_2O_3/20p composite.

4.4.3 Coefficient of friction

The variation of the friction coefficient with sliding velocity and normal stress is shown in Figure 4.16. The friction coefficient is observed to increase slightly (from 0.367 to 0.38 and 0.37 to 0.4 respectively) with the sliding velocity at the normal stresses of 2MPa and 3MPa. At 1MPa normal stress, it is found to be fluctuating. The friction

coefficient is observed to be low for lower loads but to increase for an increase of the applied loads. No significant effect of load is observed on the friction coefficient at 1m/s sliding velocity.

EDX analysis reveals the existence of increasing percentages of copper in friction film with sliding velocity at the normal stress of 2MPa (Table 4.3). A lower value of the friction coefficient (0.37 and 0.377) is observed at lower sliding velocities (1m/s and 1.5m/s) for a normal stress of 3MPa. The presence of traces of sulphur may be the reason (Table 4.3). This indicates the presence of metal sulphides, which act as a solid lubricant [17]. The friction coefficient is observed to be fluctuating with the increasing sliding velocity for 1MPa normal stress. It decreases slightly (from 0.37 to 0.35) with the increase in sliding velocity from 1m/s to 1.5m/s. EDX analysis of friction films reveals the decreasing percentage of copper (Table 4.3). This could be the reason for the decrease. With a further increase in the sliding velocity to 2m/s, the friction coefficient increases to 0.37. EDX analysis reveals an increasing percentage of copper in the friction film (Table 4.3). With an increase in the sliding velocity to 2.5m/s, the friction coefficient drops to 0.34. EDX analysis shows a lower percentage of copper in transfer film (Table 4.3). Therefore, the friction coefficient increased with the increment of copper percentages [51]. It can be inferred that the increasing and decreasing percentages of copper in friction film cause the coefficient of friction to increase and decrease. An increase in the normal stress from 1MPa to 2MPa at a sliding velocity of 2m/s does not cause any change in the friction coefficient. EDX analysis of friction film revealed the increasing percentage of copper in the friction film (Table 4.3). At the same time, sulphur and magnesium were also found at the normal stress of 2MPa. This indicates the presence

of magnesium oxide and metal sulphides. Magnesium oxide acts as an abrasive [52], and metal sulphides act as a solid lubricant [17]. Thus, it is assumed that the synergistic effect of copper, sulphur and magnesium maintained the frictional stability. An abrupt increase in the friction coefficient to 0.38 is observed with an increase in the normal stress to 3MPa. EDX analysis reveals the existence of a higher percentage of magnesium and oxygen in the friction film (Table 4.3). This indicates the presence of magnesium oxide, which acts as an abrasive [52].

Table 4.3: EDX analysis results and interface temperatures for AA6061/Al_2O_3/20p composite

	1MPa	2MPa	3MPa
1m/s	Cu-2.07%, T=64°C.	Cu-1.76% T=87°C.	Cu-5.6%, S-0.93% T=73°C.
1.5m/s	Cu-1.72% T=71°C.	Cu-8.18% T=98°C.	Cu-9.37%, S-1.25%, Mg-1.98 T=116°C.
2m/s	Cu-2.51% T=73°C.	Cu-6%, Al-14.6%, Mg-1.94%, S-1.5%, T=113°C.	Cu-6.12%, N-25.58%, Mg-6.44%, T=124°C.
2.5m/s	Cu-0.81%, S-0.29%, T=98°C.	Cu-2.32%, Mg-1.17, T=111°C.	Cu-5.39%, Mg-1.31% T=**144°C**.

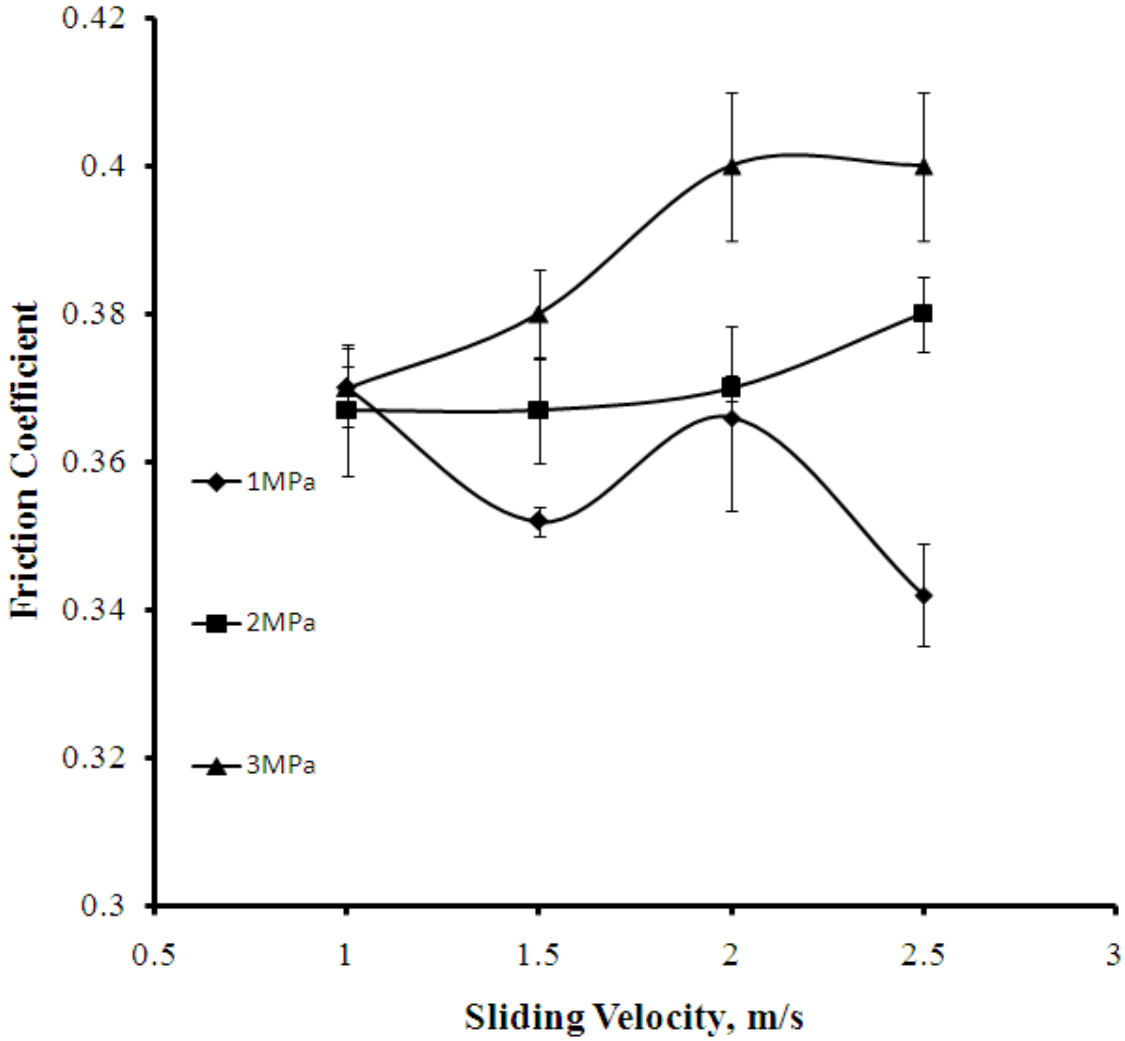

Figure 4.16 Friction coefficient for brake pad material sliding against AA6061/Al_2O_3/20p composite

4.5 Wear comparison of gray cast iron and AA6061/Al_2O_3/20p

The comparison of the wear rate of gray cast iron and AA6061/Al_2O_3/20p sliding against the semi-metallic brake pad material, under identical conditions of sliding velocity and normal stress, is shown in Figure 4.17. At the normal stress of 3MPa, the effect of sliding velocity on the wear rate of gray cast iron is observed to be 33% higher. In general, the wear rate is observed to be 18% higher for gray cast iron. For AA6061/Al_2O_3/20p, the wear is found to be 18% lower, because of the presence of hard Al_2O_3 particles in AMC, which act as load-bearing members and have an abrasive nature.

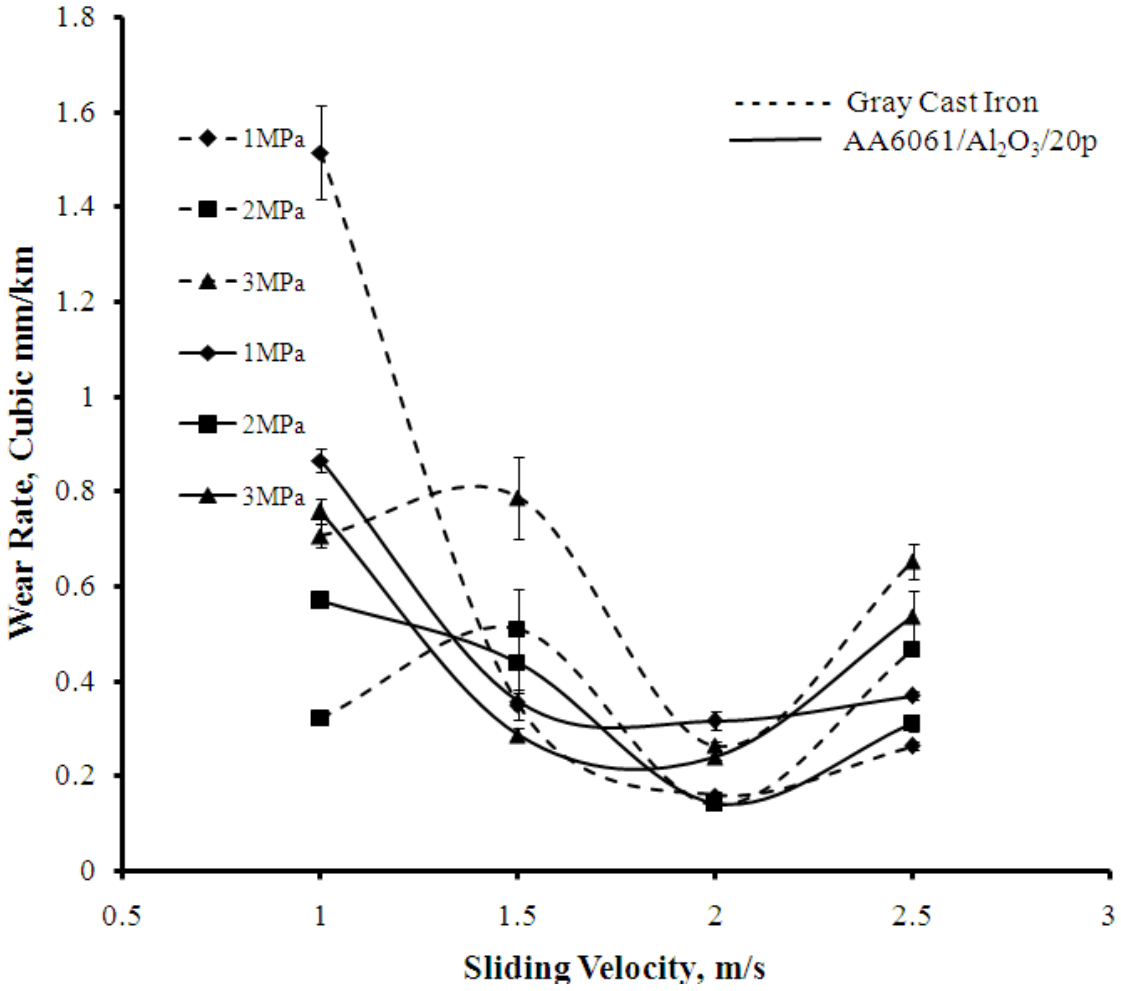

Figure 4.17 Comparison of wear rate in gray cast iron and AA6061/Al_2O_3/20p

4.6 Wear comparison in semi-metallic brake pad material

The comparison of the wear rate in the brake pad material sliding against gray cast iron and AA6061/Al_2O_3/20p counterfaces, under identical conditions of sliding velocity and normal stress, is shown in Figure 4.18. The average wear rate is observed to be 75% higher for the brake pad material while sliding against gray cast iron counterpart at the velocity of 1m/s. At the sliding velocity of 2.5m/s, the average wear rate is

observed to be 60% higher for the brake pad material while sliding against the gray cast iron counterpart. The average wear rate of the brake pad material is observed to be 60%, 50%, 20% higher while sliding against the gray cast iron counter face under the normal stresses of 1MPa, 2MPa, 3MPa respectively. The wear rate of the brake pad material is found to be 79% higher while sliding against the gray cast iron at the sliding velocity of 2.5m/s under the normal stress of 3MPa. In general, the wear rate is observed as 31% higher for the brake pad material sliding against the gray cast iron counter face. The lower wear rate of the brake pad material while sliding against AMC counterpart might be due to the incorporation of submicron Al_2O_3 particles in the Al matrix. Because of their smaller size, they might have been soft on the brake pad material. In addition, these particles anchored the transfer film for a longer time.

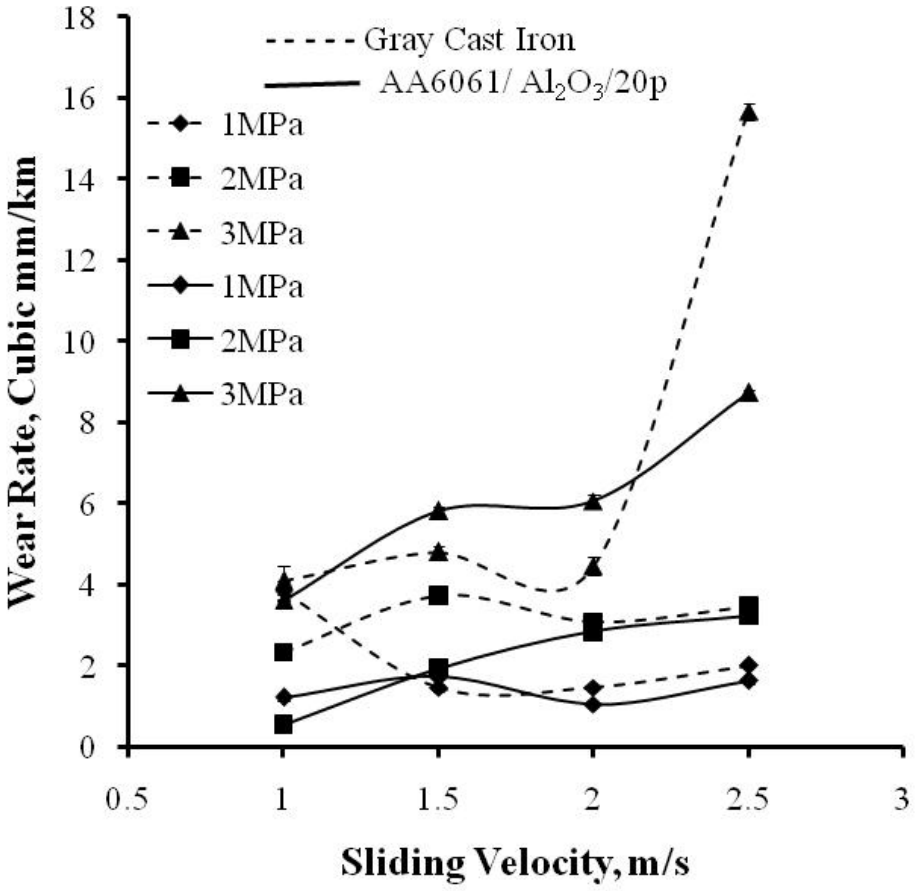

Figure 4.18 Comparison of wear rate in brake pad material against gray cast iron and AA6061/Al_2O_3/20p counterfaces

4.7 Comparison of friction coefficient

The comparison of the friction coefficient in the gray cast iron-brake pad material tribocouple and the AA6061/Al_2O_3/20p-brake pad material triocouple, under identical conditions of sliding velocity and normal stresses, is shown in Figure.4.19. The average value of the coefficient of friction with the semi-metallic brake pad material sliding against gray cast iron is found to be 20% higher than sliding against AA6061/Al_2O_3/20p composite up to 2m/s. However, its value is found to be very sensitive to loads and

sliding velocity. On the other hand, the friction coefficient of AA6061/Al_2O_3/20p is found to be very stable. At higher sliding velocities, there was no appreciable difference in coefficient of friction.

The friction coefficient generally decreases with the increment of pressure and sliding velocity for the brake pad material sliding against gray cast iron. This lowers braking force whereas a higher braking force is needed, and therefore it is an undesirable result. An abrupt increase is observed at the sliding velocity of 2.5m/s and 3MPa normal stress. This is due to degradation of the brake pad material at the elevated temperature. The maximum and minimum friction coefficient values observed are 0.535 and 0.35. The friction coefficient is observed to increase slightly with the increment of pressure and sliding velocity for the brake pad material sliding against AA6061/Al_2O_3/20p. The maximum and minimum friction coefficient values observed are 0.35 and 0.4. No fade in observed when the brake pad material slides against the AA6061/Al_2O_3/20p counterface. In addition, the variation of the friction coefficient with normal stress and sliding velocity is very small. This shows that this tribocouple shows good frictional stability over the applied range of normal stresses and sliding velocities.

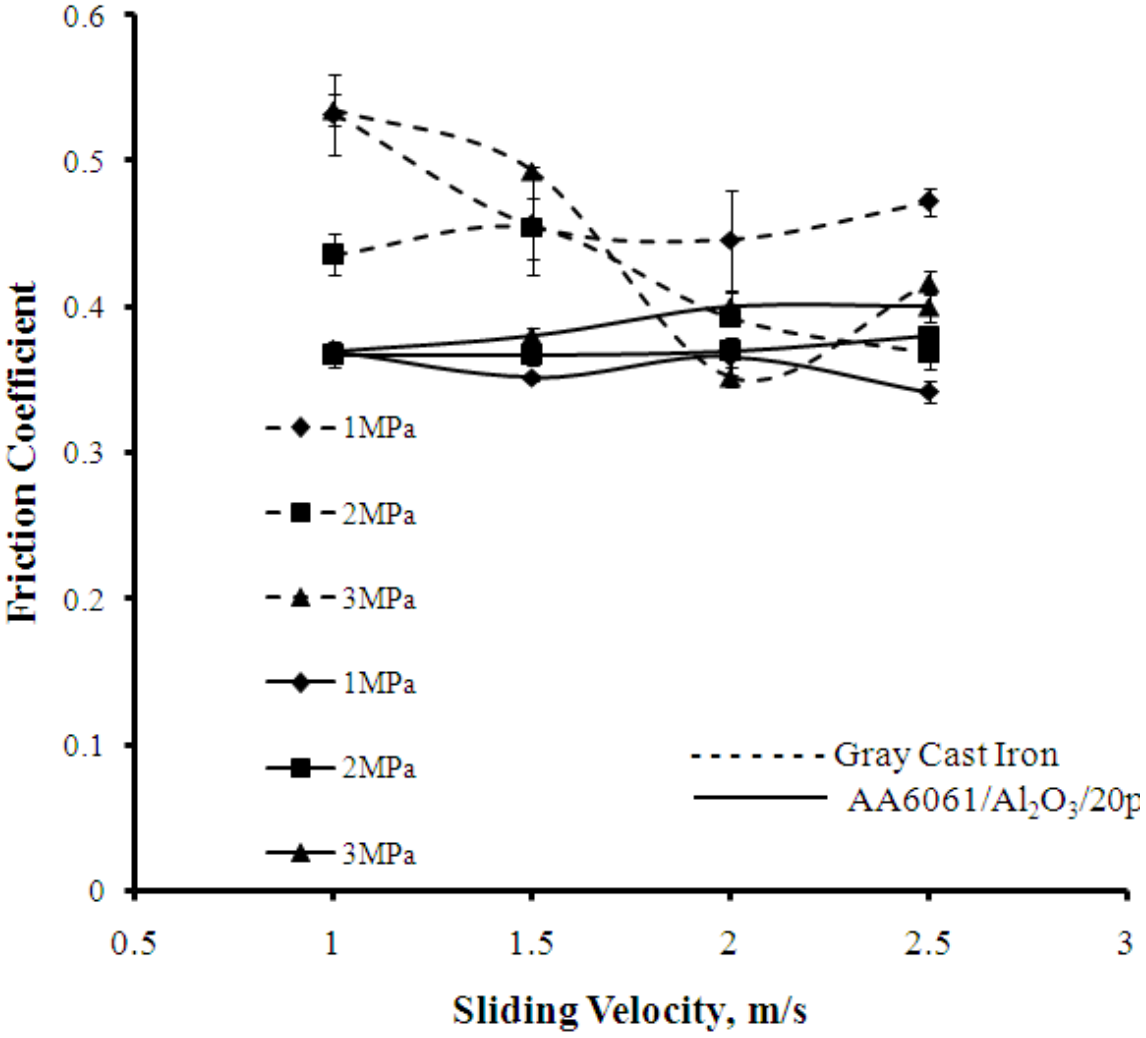

Figure 4.19 Comparison of friction coefficient with brake pad material sliding against gray cast iron and AA6061/Al_2O_3/20p counterfaces

Table 4.4 shows thermal conductivity K and specific heat C_p for gray cast iron and AA6061/Al_2O_3/20p composite. During moderate to heavy braking, thermal conductivity plays a predominant role in determining the peak rotor temperatures [30]. It follows from Table 4.4 that, as the applied pressure increases, AA6061/Al_2O_3/20p with its high thermal conductivity runs cooler and shows superior frictional stability over gray cast iron. For this reason, a low interface temperature of 144°C was observed at 3MPa

normal stress and 2.5m/s sliding velocity with AA6061/Al_2O_3/20p counterface. A higher interface temperature of 251°C was observed with the gray cast iron counterface under the identical conditions.

Table 4.4 Properties of gray cast iron and AA6061/Al_2O_3/20p composite

Material	K(W m-1 K-1)	Cp (J kg-1K-1)
Gray cast iron	39.73	480
AA6061/Al2O3/20p	55.83	1192

CHAPTER 5

5.1 Conclusions

The friction and wear behavior of 20% volume fraction sub-micron Al_2O_3 reinforced 6061 Al composite against semi-metallic brake pad material has been evaluated at varying normal stresses and sliding speeds. The results were compared with those of gray cast iron under similar conditions. Primary findings of the investigation are as follows:

1. When brake surfaces slide against one another, a friction film (transfer layer) forms on both the gray cast iron and AA6061/Al_2O_3/20p composite surfaces. Compositional characterization of the transfer layers reveals that they are heterogeneous, since the friction materials from which they form may contain in excess of 15 different additives.
2. The transfer layer acts as a protective layer for the matrix material as well as the brake pad material. Thus, the formation of the transfer layer can significantly affect the wear behavior of the tribological couple in a brake system during practical use.
3. The average wear rate of the AA6061/Al_2O_3/20p composite is found to be 18% lower than that of gray cast iron sliding against semi-metallic brake pad material.
4. The average wear rate for brake pad material is found to be 31% lower while sliding against AA6061/Al_2O_3/20p composite than sliding against gray cast iron. This can be a result of lower interface temperature of the tribocouple for the AA6061/Al_2O_3/20p composite with the brake material, compared to that for the gray cast iron with the brake material.

5. The average value of the coefficient of friction with semi-metallic brake pad material sliding against gray cast iron is found to be 20% higher than sliding against AA6061/Al_2O_3/20p composite up to 2m/s. However, its value is found to be very sensitive to loads and sliding velocity. On the other hand, the friction coefficient of AA6061/Al_2O_3/20p is found to be very stable. At higher sliding velocities, there was no appreciable difference in the coefficient of friction.
6. The AA6061/Al_2O_3/20p composite has higher wear resistance and a more stable friction coefficient than gray cast iron. Moreover, it causes less wear of the counter-face semi-metallic brake material, compared to gray cast iron.

The wear comparison study has shown that the AA6061/Al_2O_3/20p composite is a more suitable candidate material for brake rotor/disc applications, specifically at high braking power. Even though the results are optimistic, further investigations are needed for these materials before using them in commercial applications.

5.2 Future work

1. An experimental setup should be designed to slide the rotor material against the brake pad material.
2. Study the effect of varying the Al_2O_3 concentration on friction and wear behavior of the proposed brake rotor material.
3. Study the effect of cyclic loading.

REFERENCES

1. S.C.Tjong, Z.Y.Ma, "Microstructural and mechanical characteristics of in situ metal matrix composites", Material Science and Engineering, 2000, vol.29, pp 49-113.
2. L.M.Tham, M.Gupta, L.Cheng, "Influence of processing parameters on the near-net shape synthesis of aluminum-based metal matrix composites", Journal of Materials Processing Technology, 1999, vol. 89-90, pp.128-134.
3. K.K.Chawla, "Composite Materials: Science and Engineering", Second Edition, Springer, 2001.
4. Composite Materials Handbook, Vol 4, Metal Matrix Composites, Department of Defense Hand Book, U.S.A.
5. Aluminum and Aluminum Alloys, ASM Specialty Handbook, 2002, SASM International, U.S.A.
6. J.M.Torralba, C.E.Da Costa, F Velasco, F., "P/M aluminum matrix composites: an overview", Journal of Materials Processing Technology, 2003, vol.133, pp.203–206.
7. H.Nakanishi, K.Kakihara, A.Nakayama, T.Murayama, "Development of aluminum metal matrix composites (Al-MMC) brake rotor and pad", Society of Automotive Engineers of Japan, Inc. and Elsevier Science, 2002, vol.23, pp.365–370.
8. S.Zhang , F.Wang, "Comparison of friction and wear performances of brake material dry sliding against two aluminum matrix composites reinforced with different SiC particles", Journal of Materials Processing Technology, 2007, vol.182, pp.122–127.

9. N.Natarajan, S.Vijayarangan, I. Rajendran, "Wear behaviour of A356/25SiCp aluminium matrix composites sliding against automobile friction material", Wear, 2006, vol.261, pp.812–822.
10. T.W.Clyne, "Composites: MMC, CMC, PMC", A Mortensen (ed.), Encyclopaedia of Materials: Science and Technology, Elsevier, 2001.
11. M.Schwartz, Composite materials handbook, 2nd ed., McGraw-Hill, Inc., 1992.
12. V.Amigo, J.L.Ortiz, M.D.Salvador, "Microstructure and mechanical behavior of 6061Al reinforced with silicon nitride particles, processed by powder metallurgy", Scripta Materialia, 2000, vol.42, pp.383–388.
13. S. J. Harris, AGARD Lectures Series no. 174, New Light Alloys, 1990, pp. 4:1-4:21.
14. A.T.Alpas, J.Zhang, "Effect of SiC particulate reinforcement on the dry sliding wear of aluminium-silicon alloys (A356)", Wear, 1992, vol.155,pp.83-104.
15. H.Bern, "Comparison of wear resistant MMC and white cast iron", Wear, 2003, vol.254, pp.47-54.
16. M.Eriksson, F.Bergman, S.Jacobson, "On the nature of tribological contact in automotive brakes", Wear, 2002, vol.252, pp.26–36.
17. D.Chan, G.W.Stachowiak, "Review of automotive brake friction materials", J. Automobile Engineering, 2004, vol. 218, pp.953-966.
18. J.W.Kaczmar, K.Pietrzak, W.Wlosinski, "The production and application of metal matrix composite materials", Journal of Materials Processing Technology, 2000, vol.106, pp.58-67.
19. X.X.Yu, W.B. Lee, "The design and fabrication of an alumina reinforced aluminum composite material", Composites: Part A, 2000, vol.31, pp.245–258.

20. R.G. Bayer, “Mechanical Wear Prediction and Prevention”, MARCELL DEKKER, INC., 1994.
21. Q.D.Qin, Y.G.Zhao,W.Zhou, “Dry sliding wear behavior of Mg_2Si/Al against automobile friction material”, Wear,2008, vol.264, pp.654-661.
22. C.S.Ramesh, M Safiulla, “Wear behavior of hot extruded Al6061 based composites”, Wear, 2007, vol.263, pp.629-635.
23. B.N.P.Bai, B.S.Ramesh, M.K.Surappa, “Dry sliding wear of A356-Al-SiC_P composites”, Wear, 1992, vol.157, pp.295-304.
24. S.Wilson, A.T.Alpas, “Effect of temperature on the sliding wear performance of Al alloys and Al matrix composites”, Wear, 1996, vol.196, pp.270-278.
25. A.R.Nesarikar, S.N.Tewari, E.E. Graham, “Room temperature wear characteristics of Al_2O_3-particle-reinforced aluminum alloy composite”, Materials Science and Engineering, 1991, vol.147, pp.191-199.
26. S.C.Sharma, “The sliding wear behavior of Al6061–garnet particulate composites”, Wear, 2001, vol.249, pp.1036–1045.
27. M.Kok, K.Ozdin, “Wear resistance of auminium alloy and its composites reinforced by Al2O3 particles”, Journal of Materials Processing Technology, 2007, vol.183, pp.301-309.
28. G.Cueva, A.Sinatora, W.L.Guesser, A.P.Tschiptschin, “Wear resistance of cast irons used in brake disc rotors”, Wear, 2003, vol.255, pp.1256–1260.
29. S.V.Prasad, R.Asthana, “Aluminium metal-matrix composites for automotive applications: tribological considerations”, Tribology Letters,2004,vol.17, pp.445-453.

30. G.J.Howell, A.Ball, “Dry sliding wear of particulate-reinforced aluminium alloys against automobile friction materials”, Wear, 1995, vol.181-183, pp.379-390.
31. G.Straffelini, M.Pellizzari, A.Molinari, “Influence of load and temperature on the dry sliding behaviour of Al-based metal-matrix-composites against friction material”, Wear, 2004, vol.256, pp.754–763.
32. K.M.Shorowordi, A.S.M.A.Haseeb, J.P.Celis, “Velocity effects on the wear, friction and tribochemistry of aluminum MMC sliding against phenolic brake pad”, Wear, 2004, vol.256, pp.1176–1181.
33. R.K.Uyyuru, M.K.Surappa, S.Brusethaug, “Effect of reinforcement volume fraction and size distribution on the tribological behavior of Al-composite/brake pad tribo-couple”, Wear, vol.260, pp.1248–1255.
34. R.K.Uyyuru, M.K.Surappa, S.Brusethaug, “Tribological behavior of Al–Si–SiCp composites/automobile brake pad system under dry sliding conditions”, Tribology International, 2007, vol.40, pp.365–373.
35. G.Abouelmagd, “Hot deformation and wear resistance of P/M aluminium metal matrix composites”, Journal of Materials Processing Technology, 2004, vol.155–156, pp.1395–1401.
36. L.A.Dobrzanski, A.Wlodarczyk, M.Adamiak, “The structure and properties of PM composite materials based on EN AW-2124 aluminum alloy reinforced with the BN or Al_2O_3 ceramic particles”, Journal of Materials Processing Technology, 2006, vol.175, pp 186–191.
37. S.Kannan, H.A.Kishawy, “Tribological aspects of machining aluminium metal matrix composites”, Journal of Materials Processing Technology, 2008, vol.198, pp.399-406.

38. X.Wang, G.Wu, D.Sun, C.Qin, Y.Tian, "Micro-yield property of sub-micron Al_2O_3 particle reinforced 2024 aluminum composite", Materials Letters, 2004, vol.58, pp.333-336.

39. J.Longtao, G.Wu, D.Sun, Q.Zhang, J.Chen, "Microstructure and mechanical behavior of sub-micro particulate-reinforced Al matrix composites", Journal of Materials Science Letters, 2002, vol.21, pp.609-611.

40. A.M.Al-Qutub, I.M.Allam, T.W.Qureshi, "Effect of sub-micron Al_2O_3 concentration on dry wear properties of 6061 aluminum based composite", Journal of Materials Processing Technology, 2006, vol.172, pp.327–331.

41. J.Longtao, Z.Min, G.Wu, Z.Qiang, "Aging behavior of sub-micron Al_2O_{3p}/2024Al composites", Materials Science and Engineering, 2005, vol.392, pp.366-372.

42. V.Matejka, Y.Lu, Y.Fan, G.Kratosova, J.Leskova, "Effects of silicon carbide in semi-metallic brake materials on friction performance and friction layer formation", Wear, 2008, vol.265, pp.1121-1128.

43. T.Wiebgarber, "Manufacturing of Al–Al_2O_3 composite by powder metallurgy", Fraunhofer Institute Angewand Materialforschung internal report, 2000.

44. Product data sheet DP005, SCAN-PAC: 'GREEN GRIPPER', Brake & Clutch Linings, USA, 2008.

45. M.Terheci, R.R.Manory, J.H.Hensler, "The friction and wear of automotive grey cast iron under dry sliding conditions", Wear, 1995, vol.180, pp.73-78.

46. M.Eriksson, J.Lord, S.Jacobson, "Wear and contact conditions of brake pads:dynamical in situ studies of pad on glass", Wear, 2001, vol.249, pp.272–278.

47. B.Ozturk, F.Arslan, S.Ozturk, “Hot wear properties of ceramic and basalt fiber reinforced hybrid friction materials”, Tribology International, 2007, vol.40, pp.37–48.
48. J.R.Gomes, O.M.Silva, C.M.Silva, L.C.Pardini, R.F.Silva, “The effect of sliding speed and temperature on the tribological behaviour of carbon–carbon composites”, Wear, 2001, vol.249, pp.240-245.
49. T.Liu, S.K.Rhee, “High temperature wear of semimetallic disc brake pads”, Wear, 1978, vol.46, pp.213-218.
50. M.M.Morshed, A.S.M.A.Haseeb, “Physical and chemical characteristics of commercially available brake shoe lining materials: a comparative study”, Journal of Materials Processing Technology, 2004, vol.155–156, pp.1422–1427.
51. I.Mutlu, C.Oner, F.Findik, “Boric acid effect in phenolic composites on tribological properties in brake linings”, Materials and Design, 2007, vol.28, pp.480–487.
52. M.H.Cho, S.J.Kim, D.Kim, H.Jang, “Effects of ingredients on tribological characteristics of a brake lining: an experimental case study”, Wear, 2005, vol.258, pp.1682–1687.
53. S. K. Sinha, S. K. Biswas, “Friction and wear behaviour of continuous fibre as cast Kevlar-phenolic resin composite”, Journal of materials science , 1992, vol.27, pp.3085-3091.

VITA

- **Mirza Murtuza Ali Baig**
- Born in Hyderabad, India, in 1980.
- Received Bachelor of Technology (B.Tech) in Mechanical Engineering from Syed Hashim College of Science and Technology (SHCST), Jawaharlal Nehru Technological University, Hyderabad, India in 2002.
- Joined the Department of Mechanical Engineering at King Fahd University of Petroleum and Minerals (KFUPM), Dhahran, Saudi Arabia, as Research Assistant in February 2006.
- Received Master of Science (MS) in Mechanical Engineering from KFUPM in 2009.
- E-mail: mirza_murtuza@yahoo.co.in